Turbulence in a hypersonic compression ramp flow

Stephan Priebe[*] and M. Pino Martín

Department of Aerospace Engineering, University of Maryland, College Park, Maryland 20742, USA

A hypersonic shock wave/turbulent boundary layer interaction (STBLI) is investigated using direct numerical simulation (DNS). The geometry is an $8°$ compression ramp, and the flow conditions upstream of the interaction are Mach 7.2 and $Re_\theta = 3500$. Consistent with experiments at similar conditions, the flow is found to be attached in the mean, although the DNS shows that the probability of observing reversed flow on an instantaneous basis is significant. Due to the high Mach number of the flow combined with a low deflection angle, the shock angle is shallow and the shock is immersed in the boundary layer for a streamwise distance equal to several incoming boundary layer thicknesses downstream of the compression corner. The instantaneous flow structure observed in the DNS is in good qualitative agreement with filtered Rayleigh scattering images obtained experimentally that are available in the literature. The behavior of the turbulence is described based on the evolution of the Reynolds stresses, the anisotropy tensor, the wall pressure spectra, and the turbulence kinetic energy budget through the interaction. The various Reynolds stress components are found to be amplified by factors of 1.8–2.5. The heat transfer through the interaction is also investigated, as well as the relationship between the velocity and temperature fields. At the corner and for a significant distance downstream of the corner, the Reynolds analogy factor lies above values typically observed in zero-pressure-gradient hypersonic boundary layers. A common heat-transfer–pressure scaling describes the behavior observed in the DNS more accurately but with some departures near the corner. In the present attached STBLI, the strong Reynolds analogy, including the assumption of a constant turbulent Prandtl number around unity, is satisfied reasonably well in the interaction, although there are significant departures in the near-wall region.

I. INTRODUCTION

While the turbulence in transonic and supersonic shock wave/turbulent boundary layer interactions (STBLIs) has been studied extensively, there are only a few studies of the turbulence in hypersonic interactions, at Mach numbers greater than 5.

Mikulla and Horstman [1] performed two-component hot-wire measurements in Mach 7 axisymmetric, reflected STBLIs. The boundary layer developed on a centerbody that consisted of a conical forebody followed by a circular cylinder, and the shock was generated by an outer, concentric cowl. Two shock generator angles ($7.5°$ and $15°$) were considered, which resulted in attached and separated flow, respectively. The streamwise and wall-normal fluctuating velocities were measured, and the Reynolds shear stress was calculated based on the measurements. It was found that the turbulence was significantly amplified in the attached case and that the fluctuation peak moved away from the wall, as is typically observed in adverse pressure gradient flows. The separated case showed significant amplification only in the vicinity of the shock, downstream of

---

*Present address: GE Research, Niskayuna, NY 12309.

which the turbulence fluctuations rapidly returned to equilibrium levels. Bookey *et al.* [2] studied an 8° compression ramp STBLI at Mach 7.2. In addition to investigating the time-averaged flow, they also investigated the instantaneous turbulent flow structure using filtered Rayleigh scattering (FRS). The case was attached in the mean, and the shock was found to be shallow, so that the shock foot was immersed in the boundary layer for a streamwise distance equal to several incoming boundary layer thicknesses downstream of the corner. The FRS images showed that on an instantaneous basis, the shock was strongly distorted by the turbulent eddies. Schreyer *et al.* [3,4] performed particle image velocimetry (PIV) measurements for the same Mach 7.2, 8° compression ramp case that was investigated by Bookey. The PIV results showed that the wall-normal velocity fluctuations are significantly amplified through the interaction, whereas the streamwise fluctuations are only weakly amplified. As expected in adverse pressure gradient flows, the fluctuation peak moved away from the wall as had also been observed by Mikulla and Horstman [1]. Further examples of the application of PIV to hypersonic STBLI are the works of Schrijer, Scarano, and van Oudheusden [5], who investigated a Mach 7 double ramp flow, and Brooks *et al.* [6], who investigated a hollow cylinder with flare at Mach 10.

Most experiments of hypersonic STBLIs do not include turbulence measurements. Surface quantities such as the wall pressure and heat transfer are typically measured (skin friction measurements are rarer), together with mean-flow visualizations such as Schlieren images, and mean-flow surveys (see Refs. [7–17], among others). These works show that the surface heat transfer is significantly amplified through the interaction, which is an important consideration in high-speed flight applications. The relationships between the temperature and velocity field that are valid in attached, zero-pressure-gradient boundary layers break down in hypersonic STBLIs. According to the Reynolds analogy (RA), the surface heat-transfer coefficient, C_h, scales with the skin-friction coefficient, C_f: $\mathrm{RAF} = \frac{2C_h}{C_f} = \mathrm{const} \approx 1$. This relationship is satisfied relatively closely in undisturbed hypersonic boundary layers. In hypersonic STBLIs, however, significant departures from the RA are observed (see, e.g., Ref. [16]). The surface heat flux appears to scale with pressure, rather than skin friction, and several such scalings have been proposed [8,18] and were shown to match experiments (see, e.g., Refs. [12,17]). A review of heat transfer in STBLI may be found in Ref. [19].

Hypersonic STBLIs are difficult to predict accurately using common Reynolds-averaged Navier-Stokes (RANS) methods. Predictions obtained with standard turbulence models give significant errors compared to experimental data, not only for separated cases but also for attached ones. Roy and Blottner [20] reviewed hypersonic experiments and computations. They concluded that the heat transfer is particularly difficult to predict and is "often in error by a factor of four or more" [20]. Gnoffo *et al.* [21] assessed the prediction accuracy of standard turbulence models for hypersonic compression ramp interactions. They introduced an uncertainty metric that captures the total error of the computational fluid dynamics (CFD) prediction compared to reference experimental data based on the error in the three surface quantities that are typically available from experiment: the wall pressure distribution, the surface heat transfer, and the length of the separated flow. Their uncertainty metric is 55% for cases with mean-flow separation and 25% for cases without mean-flow separation [21]. High levels of error are similarly found in predictions of reflected shock interactions; see Ref. [22]. Note that prediction errors are present not only for turbulent hypersonic shock/boundary layer interactions but also for laminar ones (see, e.g., Ref. [23]).

One of the contributing reasons for the turbulence model deficiencies is the limited number of available experiments and numerical simulations that are suitable for model development and detailed validation. Settles and Dodson [24–26] reviewed supersonic and hypersonic STBLI experiments and identified 19 experiments suitable for model development and validation, of which 7 are in the hypersonic regime. The more recent review by Roy and Blottner [20] identified nine experiments. These experiments include measurements of mean surface quantities, such as the wall pressure and heat transfer, and as discussed in [20,21], off-wall and turbulence quantities, which would be useful for model development, are usually not available.

In the present work, we describe the direct numerical simulation (DNS) of an attached hypersonic compression ramp STBLI. The behavior of the turbulence through the interaction is analyzed. The
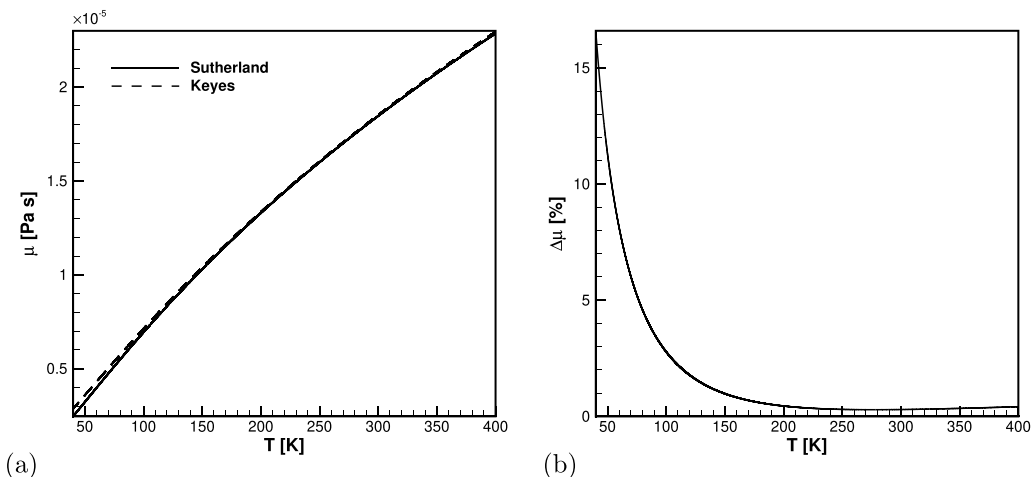
FIG. 1. Comparison between Sutherland's and Keyes' viscosity model: (a) model-predicted viscosity vs temperature, and (b) relative difference between the two models, $\Delta_\mu = \frac{\mu_{\text{Keyes}} - \mu_{\text{Sutherland}}}{\mu_{\text{Sutherland}}}$, vs temperature.

heat transfer as well as the mean and fluctuating temperature fields are also investigated, and standard relationships between the temperature and the velocity fields are assessed. We expect that the present DNS data set, which provides off-wall and turbulence quantities, may be used for developing and validating RANS and LES models, with the aim of improving predictions of hypersonic STBLI.

The paper is organized as follows: The numerical method and computational setup are presented in Sec. II. The results for the undisturbed upstream boundary layer are discussed in Sec. III A, and the results for the compression ramp interaction are discussed in Sec. III B. A summary with conclusions is given in Sec. IV.

II. NUMERICAL METHODS AND COMPUTATIONAL SETUP

The DNS code solves the compressible Navier-Stokes equations using the following numerical scheme: an optimized WENO scheme [27,28] is used for the discretization of the convective fluxes, standard fourth-order central differences for the discretization of the viscous fluxes, and a third-order low-storage Runge-Kutta scheme [29] for time integration.

The present flow conditions are low-enthalpy conditions typical of ground-based test facilities. At these low-enthalpy conditions, air behaves as a perfect gas, and we thus use the perfect gas law $p = \rho R T$ with constant specific heats. The dynamic viscosity μ is calculated using Keyes' law $\mu = 1.488 \times 10^{-6} \frac{\sqrt{T}}{1+(122.1/T)10^{-5/T}}$, where T is the temperature (in Kelvin) and μ is in Pa s [30]. Keyes' law and the commonly used Sutherland's law are compared in Fig. 1 for the range of temperatures encountered in the present flow. There are significant differences between the two viscosity models for $T < 100$ K. Since $T_\infty = 62.9$ K in the present flow, we use Keyes' law, which is more accurate at these low temperatures (see [20]). We note, however, that the temperature increases as the wall is approached where $T_w = 340$ K. The viscous stresses are largest in the near-wall region, which is at sufficiently high temperatures that the difference between the two viscosity models is small. The choice of viscosity model is thus expected to only affect the outer region of the boundary layer and the freestream, where viscous stresses tend to be small. Nevertheless, Keyes' law is more appropriate at the present conditions and is thus used in the DNS.

Regarding the computational setup, two simulations are run: (i) an undisturbed, zero-pressure-gradient, spatially developing boundary layer (auxiliary DNS), and (ii) an $8°$ compression ramp

(principal DNS). The inflow boundary condition for the principal DNS is extracted from a spanwise-wall normal plane of the auxiliary DNS.

The domain size for the auxiliary DNS is $L_x = 27\delta_{\text{ref}}$ in the streamwise direction, $L_y = 10\delta_{\text{ref}}$ in the spanwise direction, and $L_z = 14.2\delta_{\text{ref}}$ in the wall-normal direction, where $\delta_{\text{ref}} = 5$ mm is (approximately) equal to the boundary layer thickness at the inlet of the principal DNS. This is used as the reference length scale throughout the paper and is also denoted by δ (without a subscript) when nondimensionalizing. The domain is discretized with $N_x = 840$, $N_y = 768$, and $N_z = 150$ grid points for a total of 97 million. The grid resolutions based on the flow quantities at the inlet are $\Delta x^+ = 7.5$, $\Delta y^+ = 3.0$, and the first grid point from the wall is at $z^+ = 0.26$.

The domain size for the principal DNS is $L_x \approx 22.5\delta_{\text{ref}}$ (the corner is at $12\delta_{\text{ref}}$ from the inlet), $L_y = 10\delta_{\text{ref}}$, and $L_z \approx 9\delta_{\text{ref}}$, discretized with $N_x = 1060$, $N_y = 768$, and $N_z = 170$ grid points for a total of 138 million. The grid resolutions in the streamwise and spanwise directions are $\Delta x^+ = 7.0$ (inlet) to 3.2 (corner), and $\Delta y^+ = 2.8$; the first grid point from the wall is at $z^+ = 0.19$, and the resolution at the boundary layer edge is $\Delta z/\delta_{\text{ref}} = 0.036$.

Both the principal and auxiliary DNS use an isothermal, no-slip boundary condition at the wall ($T_w = 340$ K, which matches the reference experiments [4]), a periodic boundary condition in the span, and an extrapolation boundary condition at the top and outlet boundaries. The inlet boundary condition for the auxiliary DNS is specified using the rescaling method of Xu and Martín [31]; the recycling station is located at $x/\delta_{\text{ref}} = 26.0$ from the domain inlet. A time series of the flow at the recycling station is saved and used as the inflow boundary condition for the principal DNS.

Except for the change in the viscosity model described above, the present code is identical to the one that has been used in previous supersonic STBLI studies [32–34]. The same numerical approach has also been used in supersonic and hypersonic boundary layer studies [35–37]. In these previous works, the code has been validated against experiments and known analytical correlations. In addition, the present DNS is at similar conditions to the experiments by Bookey *et al.* [2] and Schreyer *et al.* [4]. Comparison to these experiments is made in Sec. III, and good overall agreement is observed. The data used for comparison include instantaneous flow visualizations, mean-flow visualizations (Schlieren), and oil-flow visualizations. A comparison between PIV data and the DNS may be found in [4].

The boundary layer DNS uses similar grid resolutions to those in previous hypersonic boundary layer calculations [35], and the STBLI DNS uses similar grid resolutions to those in previous supersonic calculations [32]. In addition, a grid convergence study for the present STBLI DNS has been performed [38], which shows that the results are converged except for a small sensitivity near the exit of the domain. In the last $3 - 4\delta_{\text{ref}}$ in the streamwise direction, C_f is higher on some of the refined grids compared to the baseline by up to 4%. In this region, the grid is somewhat coarser for two reasons: the first is that the grid is stretched in the streamwise direction toward the exit, and the second is that the wall unit $\nu_w/u_\tau = \mu_w/\sqrt{\rho_w \tau_w}$ decreases across the interaction (since both ρ_w and τ_w increase). Based on local wall units, the resolutions at a few representative locations on the ramp are $\Delta x^+ = 8$, $\Delta y^+ = 6$, and $z^+ = 0.41$ at $x/\delta_{\text{ref}} = 2$; $\Delta x^+ = 11$, $\Delta y^+ = 7$, and $z^+ = 0.47$ at $x/\delta_{\text{ref}} = 5$; and $\Delta x^+ = 18$, $\Delta y^+ = 8$, and $z^+ = 0.53$ at $x/\delta_{\text{ref}} = 10$ (just upstream of the exit). Detailed results, such as profiles of fluctuating quantities, strong Reynolds analogy terms, and turbulence kinetic energy (TKE) budgets, are only shown up to $x/\delta_{\text{ref}} = 6$ in the present paper, thus excluding the region near the exit where a grid sensitivity, although small, has been observed.

III. RESULTS

A. Upstream boundary layer

Figure 2 shows a typical instantaneous visualization of the auxiliary DNS. The variable plotted here and also in Fig. 7 is a nonlinear function of the density gradient magnitude, $e^{-10|\nabla\rho|/|\nabla\rho|_{\text{ref}}}$, which gives Schlieren-like visualizations and has been used previously (e.g., [32,34,37]). The value of $|\nabla\rho|_{\text{ref}}$ is adjusted here to be representative of large instantaneous values of $|\nabla\rho|$ encountered
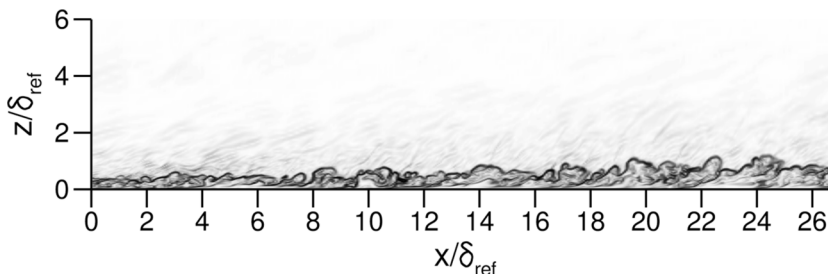
FIG. 2. Numerical Schlieren visualization of the Mach 7.2, zero-pressure-gradient boundary layer (auxiliary DNS).

in the domain, which then appear as dark regions in the visualizations. As is apparent from Fig. 2, the boundary layer grows significantly over the streamwise length of the domain. The boundary layer thickness increases from $\delta/\delta_{\rm ref} = 0.45$ at the inlet to 0.925 at the outlet. The momentum thickness increases from $\theta/\delta_{\rm ref} = 0.0175$ at the inlet to 0.0355 at the outlet, and consequently the momentum-thickness Reynolds number increases from $\mathrm{Re}_\theta = 1650$ to 3350. The displacement thickness increases from $\delta^*/\delta_{\rm ref} = 0.245$ to 0.5.

The flow conditions are listed in Table I, where the boundary layer quantities have been extracted at the recycling station, which is identical to the inlet of the principal DNS, located $12\delta_{\rm ref}$ upstream of the corner. The boundary layer profiles at this location are given in Fig. 3. These may be used to specify or verify the boundary conditions in lower-fidelity simulations, such as LES or RANS, when developing new turbulence models and validating predictions against the present DNS.

As is apparent from Fig. 4, the skin friction in the DNS follows the trend of the van Driest II prediction in the second half of the domain from $x/\delta_{\rm ref} = 13$ to the outlet, although the values of C_f in the DNS are consistently higher with an offset of $\approx 5\%$ compared to VDII [see Fig. 4(b)]. The wall in the DNS is isothermal at a temperature of 340 K. Since the recovery (or adiabatic wall) temperature is $T_r = T_\infty(1 + r\frac{\gamma-1}{2}M_\infty^2) = 645$ K (where r is taken to be 0.89), the present DNS is run with a cold wall ($T_w/T_r \approx 0.5$). The offset in the C_f compared to VDII is likely due to the low value of T_w/T_r. Duan *et al.* [36] performed temporal DNSs of Mach 5 boundary layers with varying wall temperature. For a cold wall with $T_w/T_r = 0.5$, they showed an offset of C_f in their DNS compared to VDII of approximately 5%, consistent with the present DNS. It is apparent from Fig. 4 that in the first half of the domain, from the inlet to $x/\delta_{\rm ref} = 13$, the skin friction does not follow the VDII prediction. This mismatch is due to the transient that the rescaled boundary layer undergoes until it becomes physical at around $x/\delta_{\rm ref} = 13$.

Downstream of $x/\delta_{\rm ref} = 13$, the van Driest transformed velocity profiles, which are shown in Fig. 5, follow the log law. The presence of the log law indicates that the boundary layer is fully turbulent, although the low Reynolds number causes a small wall-normal extent—at $x/\delta_{\rm ref} = 26.0$, for example, the log law extends from $z^+ = 35$ to 70. Figure 5 shows that the profiles are offset compared to the standard log law $u_{\rm VD}^+ = \frac{1}{\kappa}\ln(z^+) + B$ with $\kappa = 0.41$ and $B = 5.2$. In the present DNS, a value of $B = 5.9$ matches the data. This offset is also likely a wall temperature effect and also consistent with the findings of Duan *et al.* [36].

Figure 6 shows several spectra at the recycling station. The spectra show a broadband peak around frequencies $O(U_\infty/\delta)$, which are associated with the large-scale, energy-carrying turbulent eddies. Crucially, no spurious energy is present at the frequency characteristic of the rescaling,

TABLE I. Flow conditions.

M_∞	Re_θ	δ^+	δ (mm)	δ^* (mm)	θ (mm)	U_∞ (m/s)	u_τ (m/s)	p_∞ (Pa)	T_∞ (K)
7.21	3.3×10^3	2.1×10^2	4.58	2.48	0.175	1146.1	62.5	1341.0	62.9
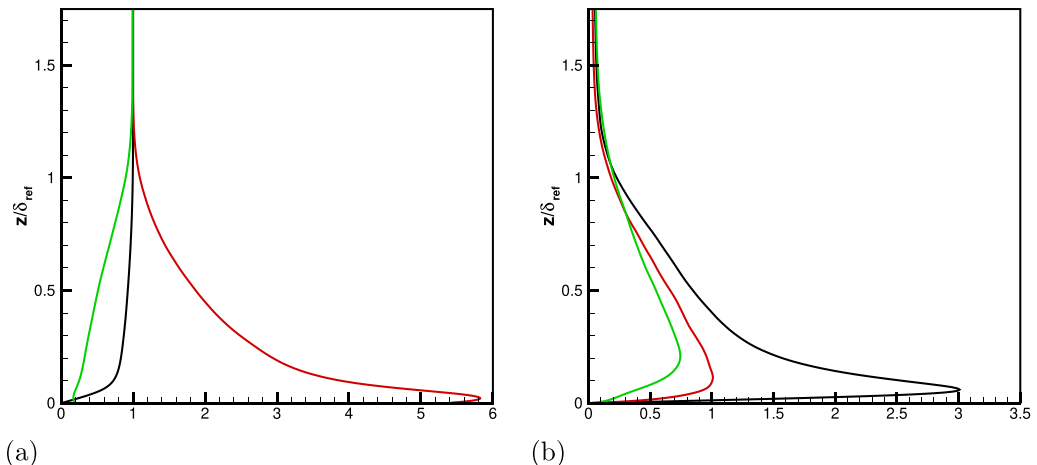
FIG. 3. Upstream boundary layer profiles. (a) $\overline{\rho}$ (green), $\tilde{u}$ (black), and $\tilde{T}$ (red); (b) $\frac{\sqrt{\widetilde{u''u''}}}{u_\tau}$ (black), $\frac{\sqrt{\widetilde{v''v''}}}{u_\tau}$ (red), and $\frac{\sqrt{\widetilde{w''w''}}}{u_\tau}$ (green).

which is $f_{\text{resc}} \approx \frac{U_\infty}{26\delta_{\text{ref}}}$. This shows that the rescaling length is chosen large enough to eliminate any artificial correlation due to the rescaling boundary condition.

The present section has provided an overview of the auxiliary DNS and presented the main results; further details may be found in [39].

B. Compression ramp

1. Instantaneous and time-averaged flow structure

Figure 7 shows two typical instantaneous visualizations from the DNS. Due to the high Mach number of the flow, combined with a low deflection angle, the shock angle is shallow (inviscid
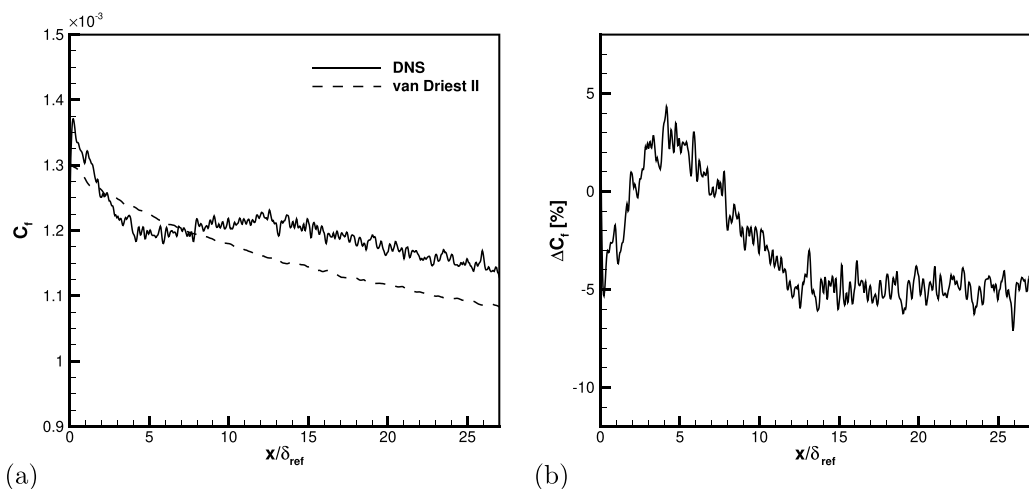

FIG. 4. (a) Time- and spanwise-averaged skin-friction coefficient in the upstream boundary layer (auxiliary DNS) as a function of the streamwise coordinate; (b) relative difference between the van Driest II prediction and the DNS, $\Delta_{Cf} = \frac{C_{f,\text{VDII}} - C_{f,\text{DNS}}}{C_{f,\text{DNS}}}$.
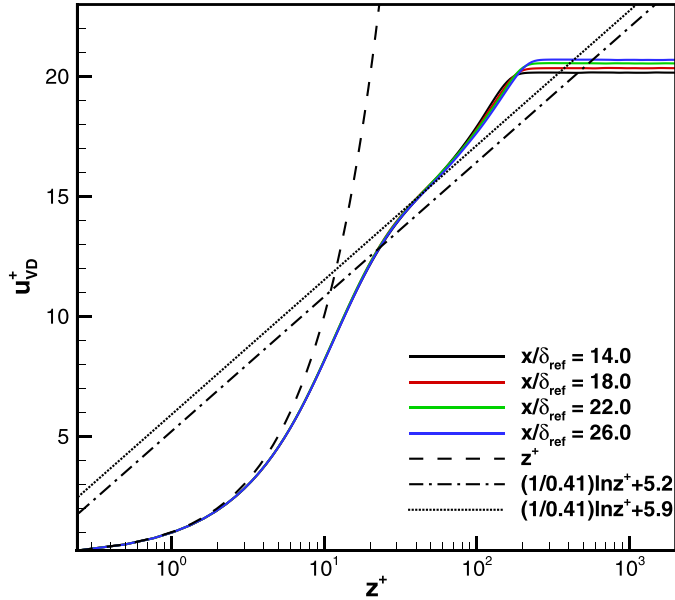
FIG. 5. Van-Driest-transformed velocity profiles in the upstream boundary layer.

value: $14.3°$). As a result, the shock is immersed in the boundary layer in the vicinity of the corner. A distinct shock sheet typically only appears in the freestream, above the turbulent eddies, at a streamwise distance equal to several incoming boundary layer thicknesses downstream of the corner. As is apparent from Fig. 7, the shock is distorted by the passage of the δ-scale turbulent bulges from the incoming boundary layer. Since these bulges carry lower momentum fluid than the irrotational freestream fluid, the shock relaxes upstream as a bulge travels through it, causing δ-sized "ripples" in the shock sheet. These ripples result in a shock sheet that appears to conform to the boundary layer bulges for up to 10δ downstream of the corner. In Fig. 7(a), for example, the shock shows the imprint of four δ-sized eddies that have convected through it and that are visible in the boundary layer on the ramp: the first bulge and corresponding imprint on the shock are visible from approximately $x/\delta_{ref} = 13.75$ to 14.5, the second from $x/\delta_{ref} = 14.75$ to 15.75, the third from $x/\delta_{ref} = 16.25$ to 17.25, and the fourth from $x/\delta_{ref} = 18.0$ to 19.0.

Figure 8 shows an instantaneous three-dimensional visualization from the DNS. The three-dimensional nature of the "ripples" in the shock sheet is visible. Since these ripples are caused by the convection of the turbulent bulges from the incoming boundary layer through the shock, the spanwise length scale of the ripples is comparable to that of the bulges and thus of $O(\delta)$. It is also apparent that further downstream toward the exit of the computational domain, the imprint of the turbulent bulges on the shock weakens. The intersection of the shock sheet with the exit boundary of the domain is fairly uniform across the span.

The present instantaneous flow structure is in qualitative agreement with the filtered Rayleigh scattering (FRS) visualizations obtained by Bookey *et al.* [2]; see Fig. 9. The boundary layer bulges appear as dark regions in the FRS images, and the shock is visible as a sharp change from gray in the freestream upstream of the shock to light gray or white downstream. As in the DNS, the shock in the experiment is shallow, immersed in the boundary layer, and once it emerges from the boundary layer it shows the "imprint" of the δ-sized turbulent bulges that have convected through it.

The mean shock structure from DNS is shown in Fig. 10. It is apparent that in the time-averaged sense, the shock is essentially attached at the corner. The shock angle at the exit of the computational domain is approximately $13.5°$, which is approaching the inviscid value of $14.3°$. The mean shock
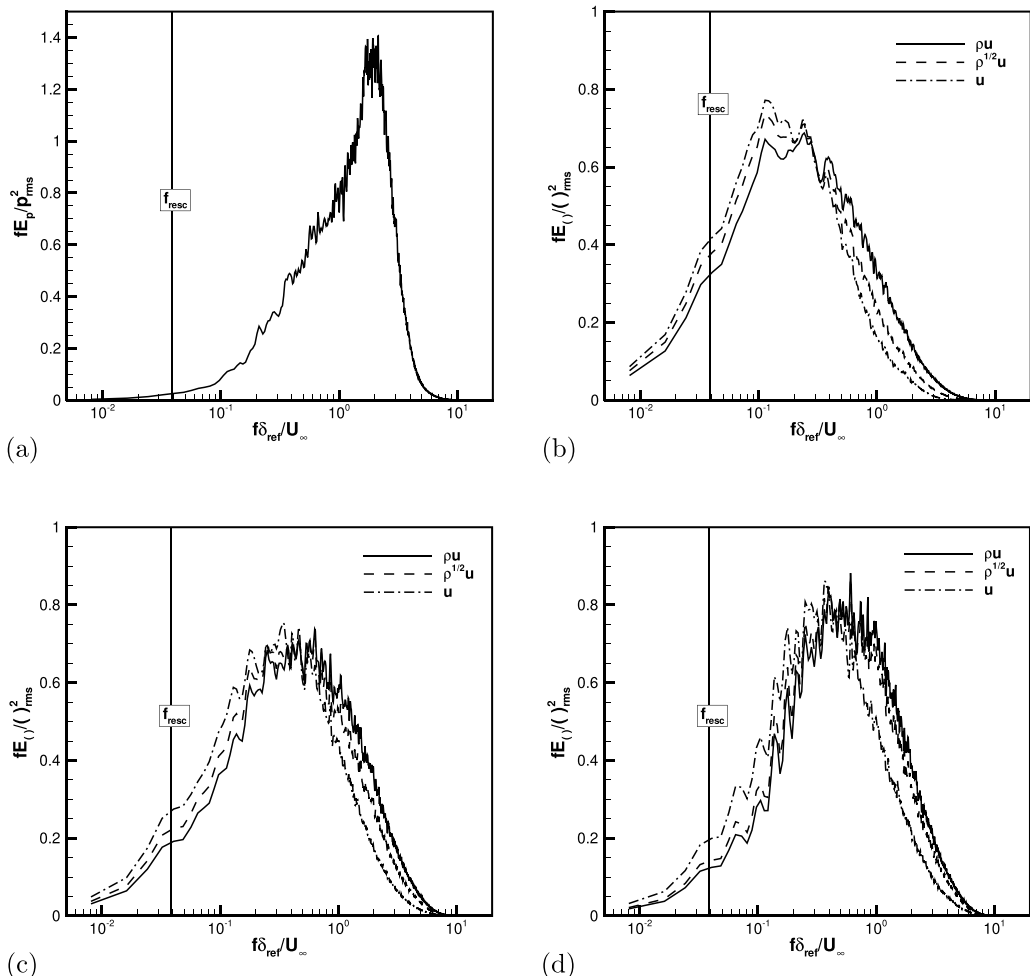
FIG. 6. Spectra in the upstream boundary layer at $x/\delta_{\mathrm{ref}} = 26.0$: (a) wall pressure, (b)–(d) streamwise velocity, momentum, and Morkovin-type scaled velocity at $z^+ = 15$ (b), $z^+ = 50$ (c), and $z/\delta_{\mathrm{ref}} = 0.5$ (d). The nominal frequency of the rescaling boundary condition, $f_{\mathrm{resc}} = \frac{U_\infty}{26\delta}$, is shown on the spectra.

structure observed in the DNS is in agreement with the corresponding experimental Schlieren visualizations in [4], which also show the time-averaged shock to be attached at the corner.

2. Surface quantities

The time- and spanwise-averaged wall pressure distribution is shown in Fig. 11(a). The ratio of the downstream-to-upstream wall pressure is $p_d/p_u \approx 3.45$, which is close to the inviscid value of 3.51. The slightly lower pressure ratio in the DNS is consistent with the observation made from Fig. 10 that the shock angle is lower than the inviscid value. The present domain extends $10.5\delta_{\mathrm{ref}}$ downstream of the corner, and while this is sufficient to give a shock strength close to the inviscid one, an even longer computational domain would be required to reach the full inviscid strength of the shock, as is often also the case in supersonic interactions (see, e.g., [32,34]).

The time- and spanwise-averaged skin friction coefficient C_f is shown in Fig. 11(c). While the value of C_f decreases significantly upstream of the corner, it does not fall below $C_f = 0$, which
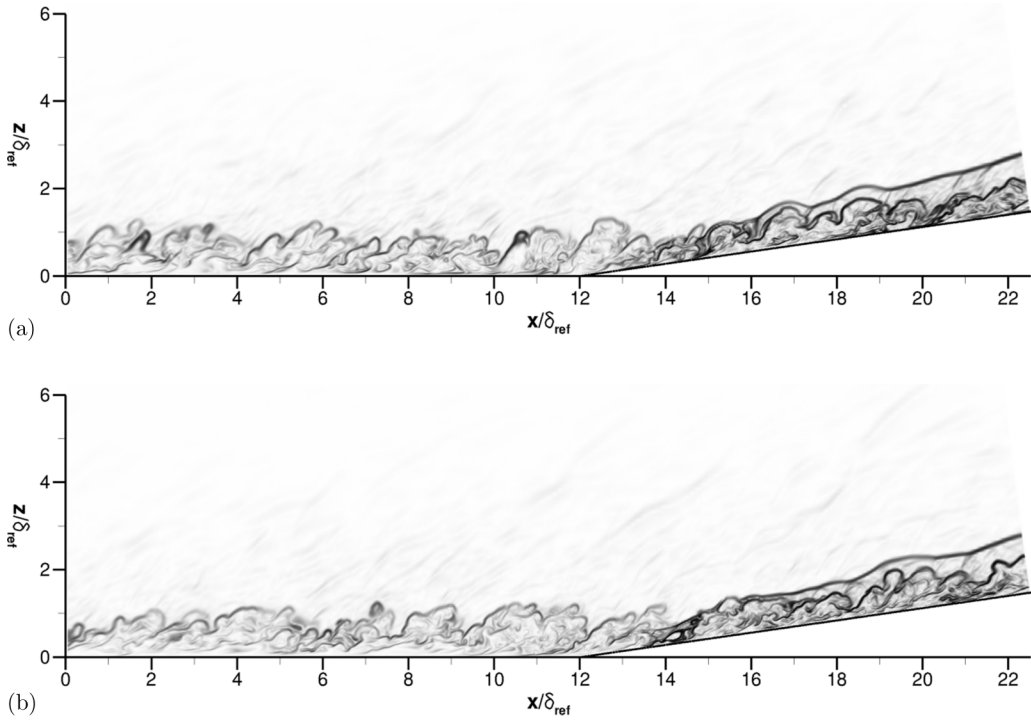
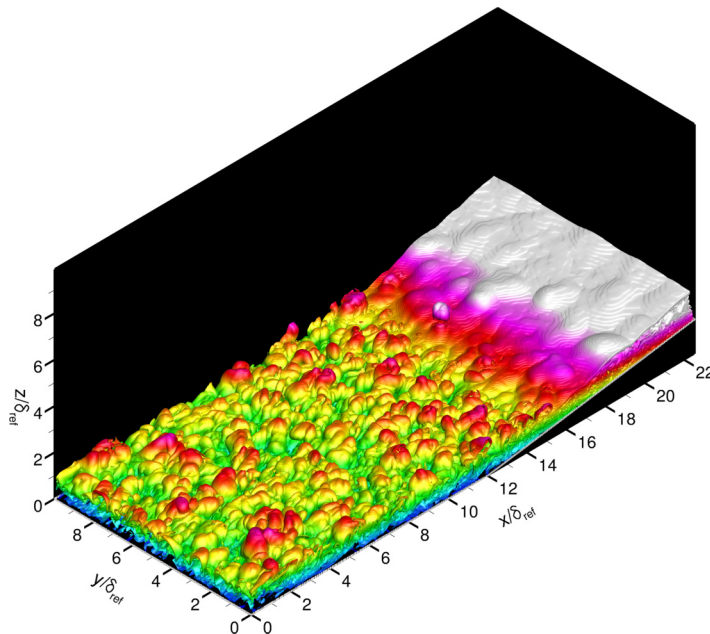FIG. 7. Numerical Schlieren visualizations of the $8°$ compression-ramp STBLI (principal DNS).

FIG. 8. Instantaneous, three-dimensional flow structure. Isosurface of the magnitude of the density gradient, colored by the wall-normal coordinate.
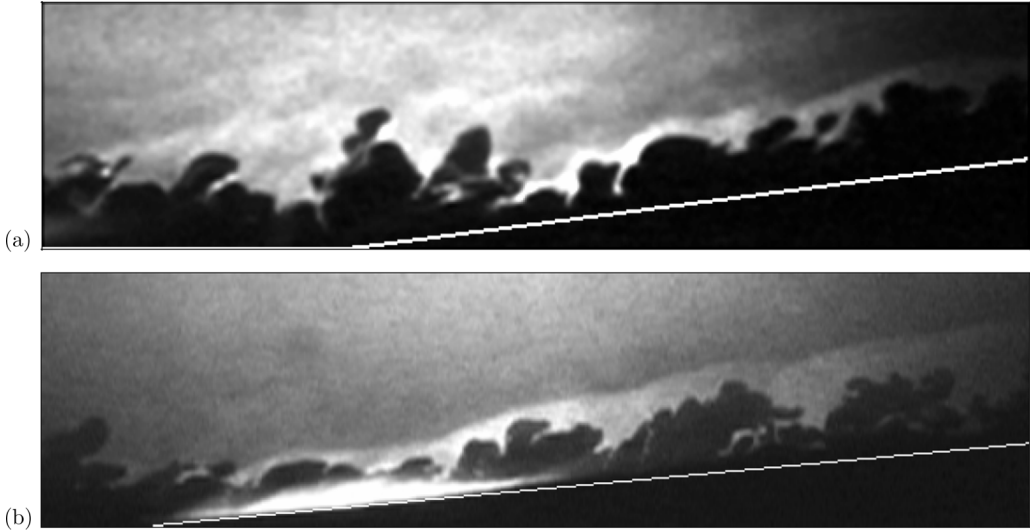
FIG. 9. Filtered Rayleigh scattering images of the $8°$ compression-ramp interaction. Reproduced from Bookey *et al.* [2]; see also Schreyer *et al.* [4].

indicates that the flow is attached in the mean. Attached flow was also observed in the experiments, as may be seen from the oil flow visualizations in [2].

The third surface quantity of interest is the heat-transfer coefficient, or Stanton number, which is defined as $C_h = \frac{q_w}{\rho_\infty U_\infty C_p (T_w - T_r)}$, where q_w is the wall heat transfer, T_w is the wall temperature, T_r is the recovery temperature, and ρ_∞ and U_∞ are the density and velocity in the freestream. Figure 11(d) shows the time- and spanwise-averaged C_h distribution. The value of C_h has a minimum at the corner before increasing to a higher level in the downstream flow compared to the upstream flow; the ratio of downstream-to-upstream heat transfer is $C_{h,d}/C_{h,u} = 2.5$.

An interesting feature of the C_f and C_h distributions is the presence of inflection points and local maxima and minima in the downstream flow. C_h, for example, shows local maxima at $x/\delta_{\rm ref} \approx 2$ and 6.5. The resulting "scalloped" shape of the distributions has also been observed by Murray *et al.* [17] in experiments of an attached axisymmetric reflected STBLI at Mach 9, where it was attributed to the nonequilibrium evolution of the boundary layer as it is subjected to a pressure
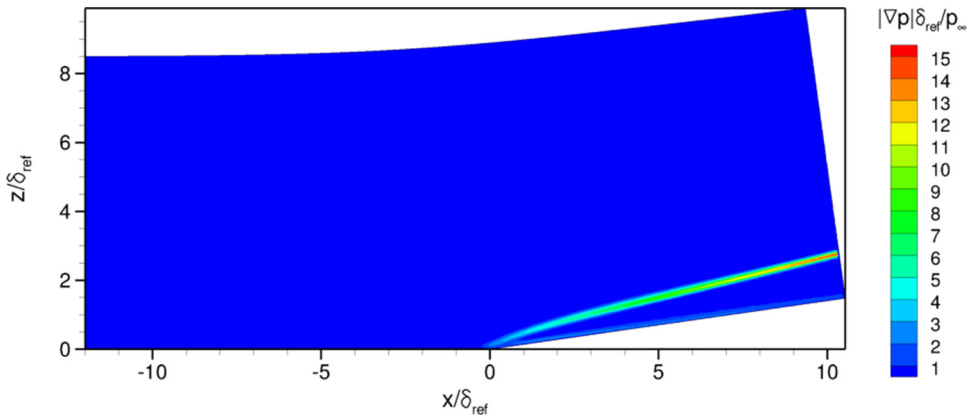

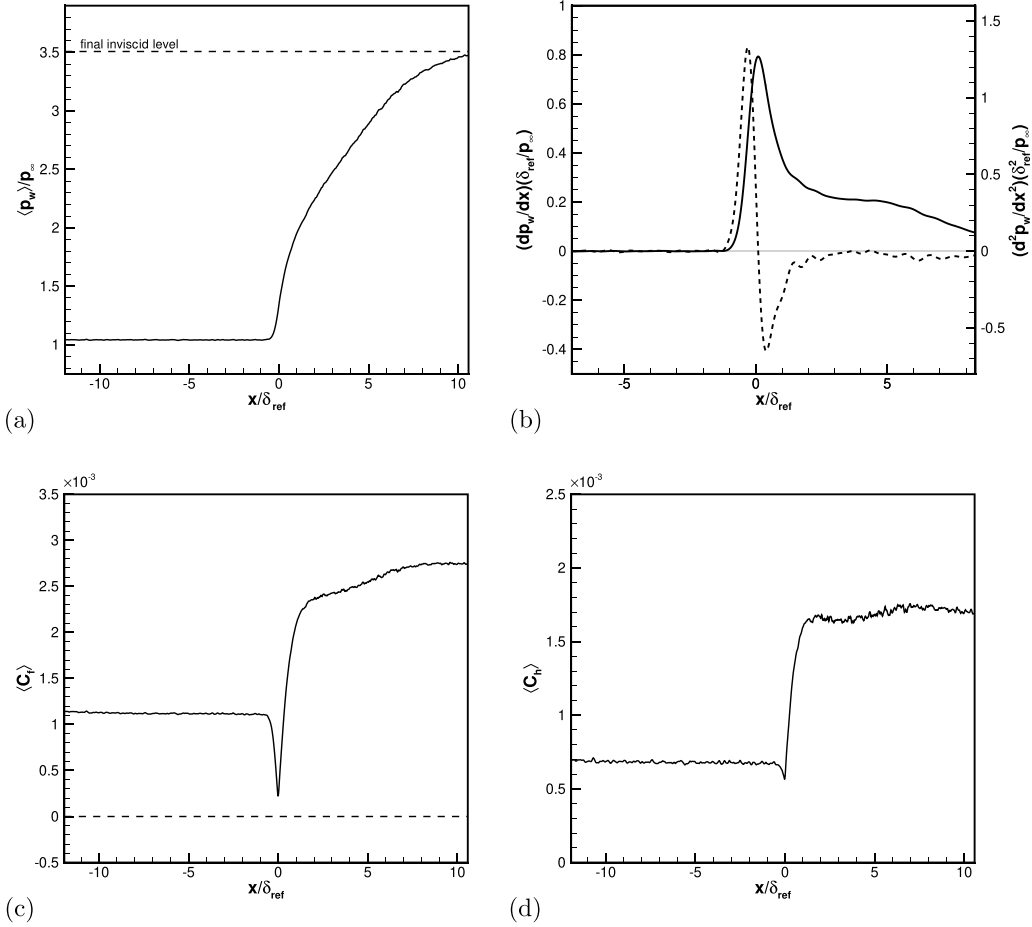FIG. 10. Time- and spanwise-averaged pressure gradient magnitude.

FIG. 11. Time- and spanwise-averaged surface quantities through the interaction: (a) wall pressure, (b) first derivative (solid) and second derivative (dashed) of the wall pressure with respect to the streamwise coordinate x, (c) skin-friction coefficient, and (d) Stanton number.

gradient that changes with streamwise distance. Such a link between the scalloped shape of C_f and C_h and changes in the pressure gradient also appears to exist in the present DNS. As is apparent from Fig. 11(b), the pressure distribution has an approximately constant slope (and hence zero curvature) between $x/\delta_{\mathrm{ref}} \approx 2$ and 6.5, and these locations correspond closely to the peaks of the scalloping in C_f and C_h.

3. State of separation

As discussed in Sec. III B 2, the time- and spanwise-averaged skin-friction coefficient C_f is greater than zero everywhere in the interaction, and the flow is thus attached in the mean. The probability of observing reversed flow on an instantaneous basis is, however, significant. It is apparent from Fig. 12, which shows a typical contour plot of the instantaneous value of C_f, that the flow is mostly attached in the upstream boundary layer, although small patches of local flow reversal are visible. Near the corner, between approximately $x/\delta_{\mathrm{ref}} = 11.5$ and $x/\delta_{\mathrm{ref}} = 12.5$, relatively large regions of reversed flow are visible. These regions can extend up to approximately $0.5\delta_{\mathrm{ref}}$ in the streamwise and spanwise directions, and they appear to be uniformly distributed across the span of the computational domain. Further downstream, in the out-of-equilibrium boundary layer on the
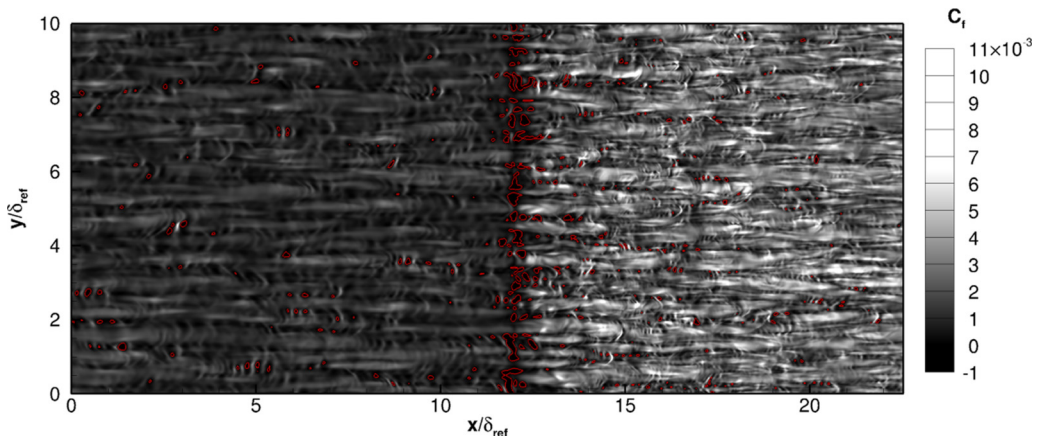
FIG. 12. Instantaneous contours of the skin-friction coefficient C_f. The red line is the $C_f = 0$ contour.

ramp, the size and number of the reversed flow regions gradually decrease with increasing distance from the corner.

The spanwise-averaged probability $\overline{\gamma}_u$ of flow reversal ($u < 0$) is shown in Fig. 13 (note that the overbar indicates spanwise-averaging). Following Simpson [40], the state of separation may be classified based on the observed values of γ_u: The flow is said to be in the *incipient detachment (ID)* state when $\gamma_u = 0.01$, i.e., when the flow is reversed 1% of the time; it is said to be in the *intermittent transitory detachment (ITD)* state when $\gamma_u = 0.2$; and in the *transitory detachment (TD)* state when $\gamma_u = 0.5$. It is apparent from Fig. 13(a) that the flow in the vicinity of the corner is in the ITD state. The values of $\overline{\gamma}_u$ lie above the ITD threshold of 0.2 in a streamwise window of approximately $0.25\delta_{\text{ref}}$ surrounding the corner (between $x/\delta_{\text{ref}} = 11.85$ and 12.1). The maximum value of $\overline{\gamma}_u$ is observed at the corner and is 0.31. Figure 13(a) also shows that $\overline{\gamma}_u$ crosses the ID threshold from below at $x/\delta_{\text{ref}} = 11.5$ (or $0.5\delta_{\text{ref}}$ upstream of the corner), and from above at $x/\delta_{\text{ref}} = 13.75$ (or $1.75\delta_{\text{ref}}$ downstream of the corner). Figure 13(b) shows that the region, in which significant nonzero values of $\overline{\gamma}_u$ are observed, is thin; at its highest point above the wall, the $\overline{\gamma}_u = 0.02$ contour line extends to approximately $(z - z_{\text{wall}})/\delta_{\text{ref}} = 0.04$. The present analysis of the reversed flow structure and probability in a hypersonic STBLI may be compared to similar analyses in the literature for lower Mach number cases; see Na and Moin [41], who investigated an incompressible separation bubble using DNS, and Pirozzoli *et al.* [42], who investigated an incipiently separated transonic STBLI using DNS.

While Fig. 13 shows the spanwise-averaged probability of flow reversal, Fig. 14 shows the three-dimensional probability. The isosurface corresponding to the ID threshold $\gamma_{u,\Delta T} = 0.01$ is shown in Fig. 14(a), and the isosurface corresponding to the ITD threshold $\gamma_{u,\Delta T} = 0.2$ is shown in Fig. 14(b). Despite the significant time duration of the present DNS of $\Delta T = 94.4\delta/U_\infty$, the isosurfaces shown in Fig. 14 are not fully converged. Following the nomenclature used in [41], the dependence of the flow reversal probability on the particular averaging time chosen is emphasized by the subscript ΔT. It is apparent from Fig. 14 that both the ID and ITD isosurfaces show some variation in the spanwise direction. The structure of the ID isosurface may be described as streaky, and the ITD isosurface is made up of distinct patches that are distributed across the span of the domain.

Note that while the three-dimensional probability in Fig. 14 is not fully converged, the other statistics shown in this paper, including the flow reversal probability in Fig. 13, are spanwise-averaged and have been verified to be converged by comparing statistics for the full DNS to those for half the time duration.
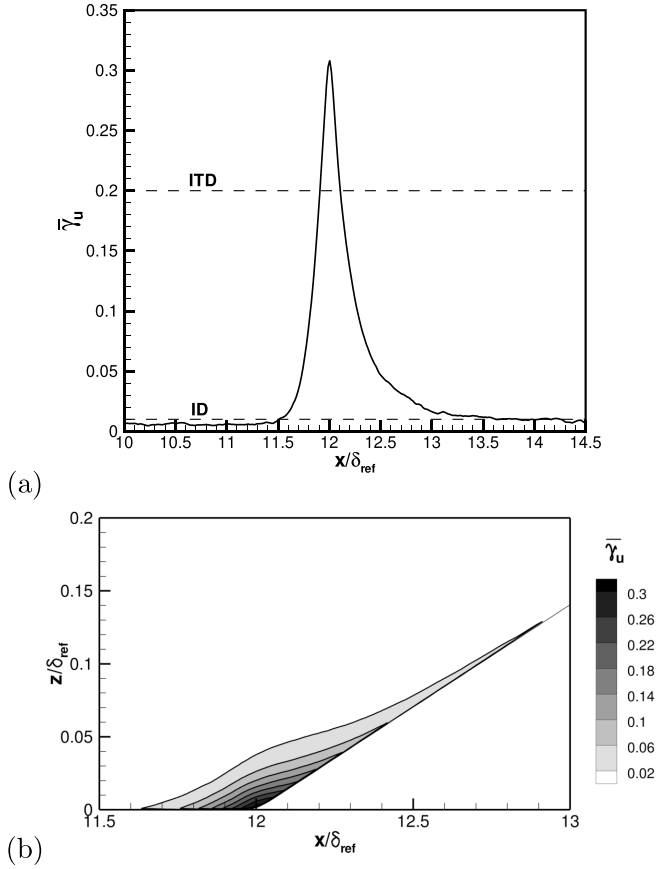
FIG. 13. Spanwise-averaged probability $\overline{\gamma}_u$ of flow reversal: (a) at the first grid point above the wall, and (b) in the streamwise–wall-normal plane.

4. Mean-flow field

Figure 15 shows the mean profiles of u-velocity, w-velocity, density, and temperature at six streamwise locations. The profiles have been extracted along the wall normal, and the streamwise coordinate given for the profiles on the ramp is the coordinate at the ramp wall. While not separated in the mean, the near-wall flow is significantly decelerated as the corner is approached. The $\tilde{u}$ profiles at three streamwise locations (upstream of, at, and downstream of the corner) are shown in Fig. 16 to highlight the changes in the profiles through the interaction. There is a significant near-wall deficit of $\tilde{u}$ at the corner, and the profile has an inflection point as typically seen in adverse pressure gradient flows. Note that in the present flow, the inflection point is located close to the wall, at $(z - z_w)/\delta_{\text{ref}} = 0.045$, consistent with the fact that the region where a significant probability of reversed flow is observed is also low. Downstream of the corner, the profiles quickly recover as shown by the profile at $x/\delta_{\text{ref}} = 1$ in Fig. 16, which does not have an inflection point. The mean wall-normal velocity $\tilde{w}$ is essentially zero in the upstream boundary layer [Fig. 15(a)] and jumps to a positive value downstream of the shock [Figs. 15(c)–15(f)] due to the deflection of the flow. The jump in $\overline{\rho}$ and $\tilde{T}$ across the shock is also visible, occurring at an increasing wall-normal distance as x is increased, corresponding to the average shock position: for example, the jump is visible at $z/\delta_{\text{ref}} \approx 0.8$ at $x/\delta_{\text{ref}} = 2.0$, and $z/\delta_{\text{ref}} \approx 1.8$ at $x/\delta_{\text{ref}} = 6.0$. The increase in $\overline{\rho}$ is more pronounced than the one in $\tilde{T}$ consistent with inviscid theory, according to which $\frac{\rho_2}{\rho_1} = 2.32$ and $\frac{T_2}{T_1} = 1.51$.
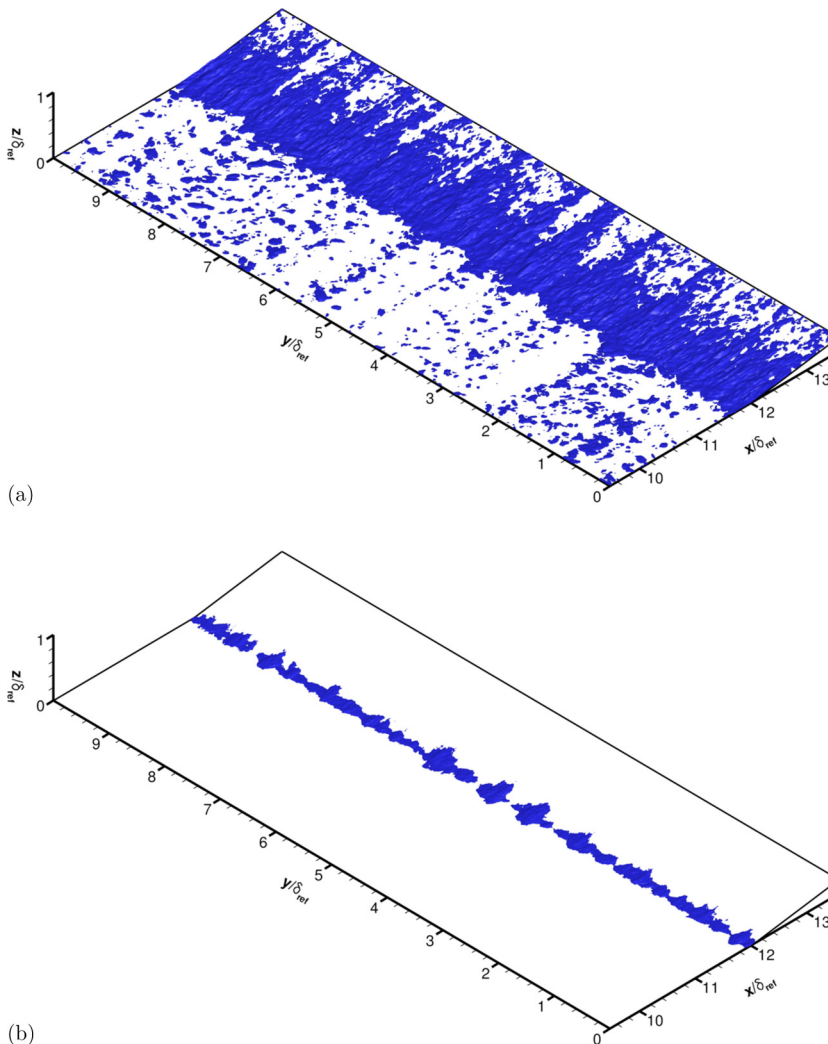
FIG. 14. Probability of flow reversal: (a) isosurface $\gamma_{u,\Delta T} = 0.01$, and (b) isosurface $\gamma_{u,\Delta T} = 0.2$.

The velocity components shown in Figs. 15 and 16 are in the (x, y, z) coordinate system, which is aligned with the upstream wall. Downstream of the corner, the ramp-aligned (x_r, y, z_r) coordinate system (rotated by $8°$) may be used. Figure 17 shows a comparison of the mean velocity components in both coordinate systems at several streamwise locations downstream of the corner. Since the ramp angle is shallow at $8°$, $\tilde{u}$ and $\tilde{u}_r$ are essentially identical. As expected, the $\tilde{w}$ and $\tilde{w}_r$ profiles are shifted [in the freestream, the shift is $-U_\infty \sin(8°)$] but the shape of the profiles is similar. There are, however, some differences: for example, $\tilde{w}$ shows a near-wall maximum at $(z - z_w)/\delta_{\text{ref}} \approx 0.05$, while $\tilde{w}_r$ does not. In what follows, the mean and fluctuating velocity components are usually taken in the ramp-aligned coordinate system when plotting quantities downstream of the corner. One exception is the Reynolds stress contours for the entire domain, which will be shown in Fig. 18. These are based on the upstream coordinate system to avoid the discontinuity at the corner that would result from a change in the coordinate system there. It has been verified that the differences between quantities in the two coordinate systems are generally small, consistent with the low ramp angle of $8°$.
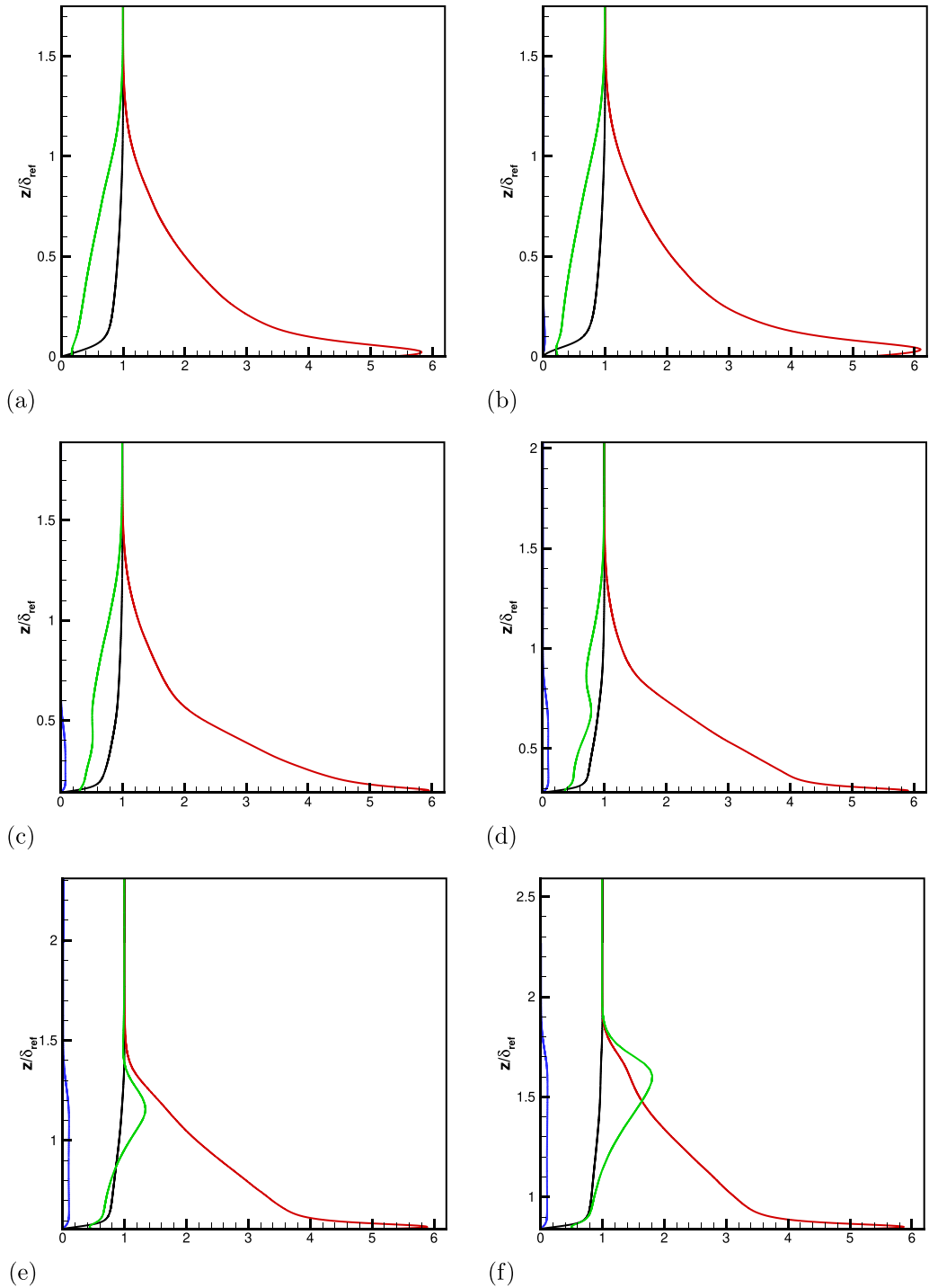
FIG. 15. Profiles of $\overline{\rho}$ (green), $\tilde{u}$ (black), $\tilde{w}$ (blue), and $\tilde{T}$ (red) through the interaction (a) $x/\delta = -4.0$, (b) $x/\delta = 0.0$, (c) $x/\delta = 1.0$, (d) $x/\delta = 2.0$, (e) $x/\delta = 4.0$, and (f) $x/\delta = 6.0$.
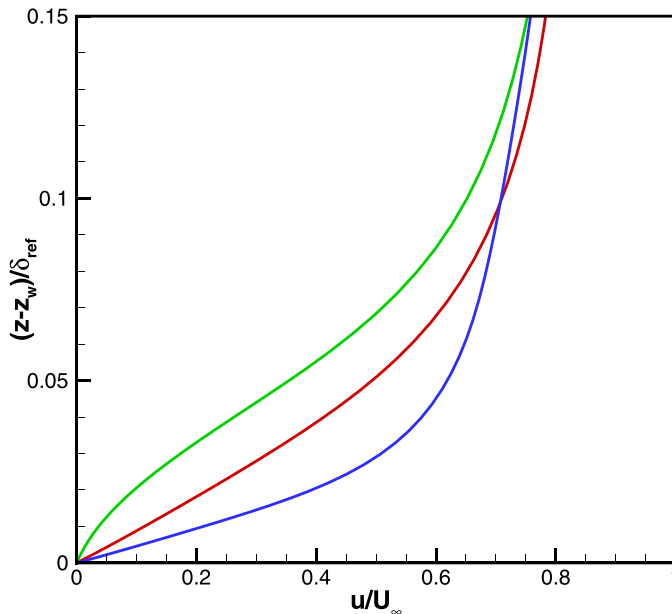
FIG. 16. Near-wall detail of profiles of streamwise velocity $\tilde{u}$ at $x/\delta_{\text{ref}} = -4$ (red), $x/\delta_{\text{ref}} = 0$ (green), and $x/\delta_{\text{ref}} = 1$ (blue).

5. *Turbulence behavior through the interaction*

Figure 18 shows contours of the Favre-averaged Reynolds stresses; the normal stresses $\widetilde{u''u''}$, $\widetilde{v''v''}$, $\widetilde{w''w''}$, and the shear stress $\widetilde{u''w''}$ are shown. It is apparent that the Reynolds stresses are amplified in the interaction region, which may be quantified by considering the amplification tensor $A_{i,j} = \frac{\max_d(\widetilde{u_i''u_j''})}{\max_u(\widetilde{u_i''u_j''})}$ $(i, j = 1, 2, 3)$, i.e., the ratio of the maximum value of a particular component
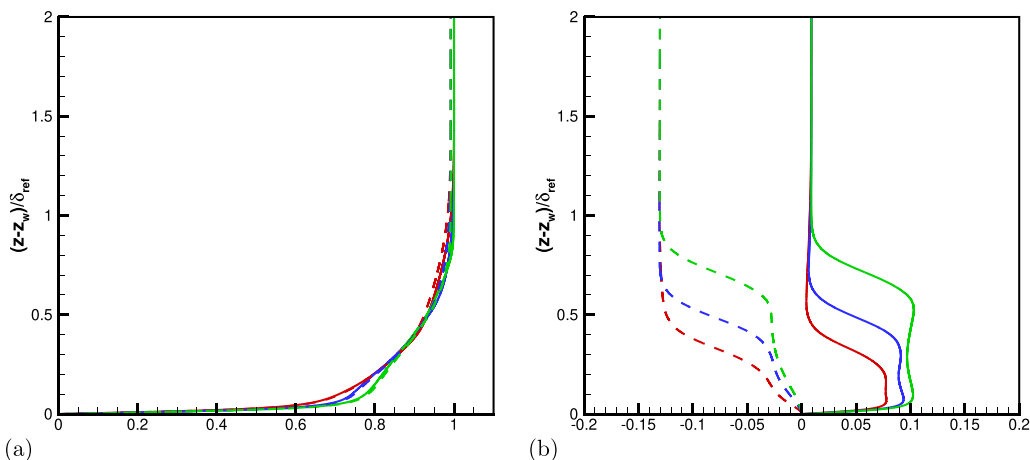

FIG. 17. Comparison of the mean velocity profiles in the (x, y, z) coordinate system aligned with the upstream wall and the (x_r, y, z_r) coordinate system aligned with the ramp: (a) $\tilde{u}$ (solid) vs $\tilde{u}_r$ (dashed), and (b) $\tilde{w}$ (solid) vs $\tilde{w}_r$ (dashed). The streamwise locations shown are $x/\delta_{\text{ref}} = 1$ (red), $x/\delta_{\text{ref}} = 2$ (blue), and $x/\delta_{\text{ref}} = 4$ (green).
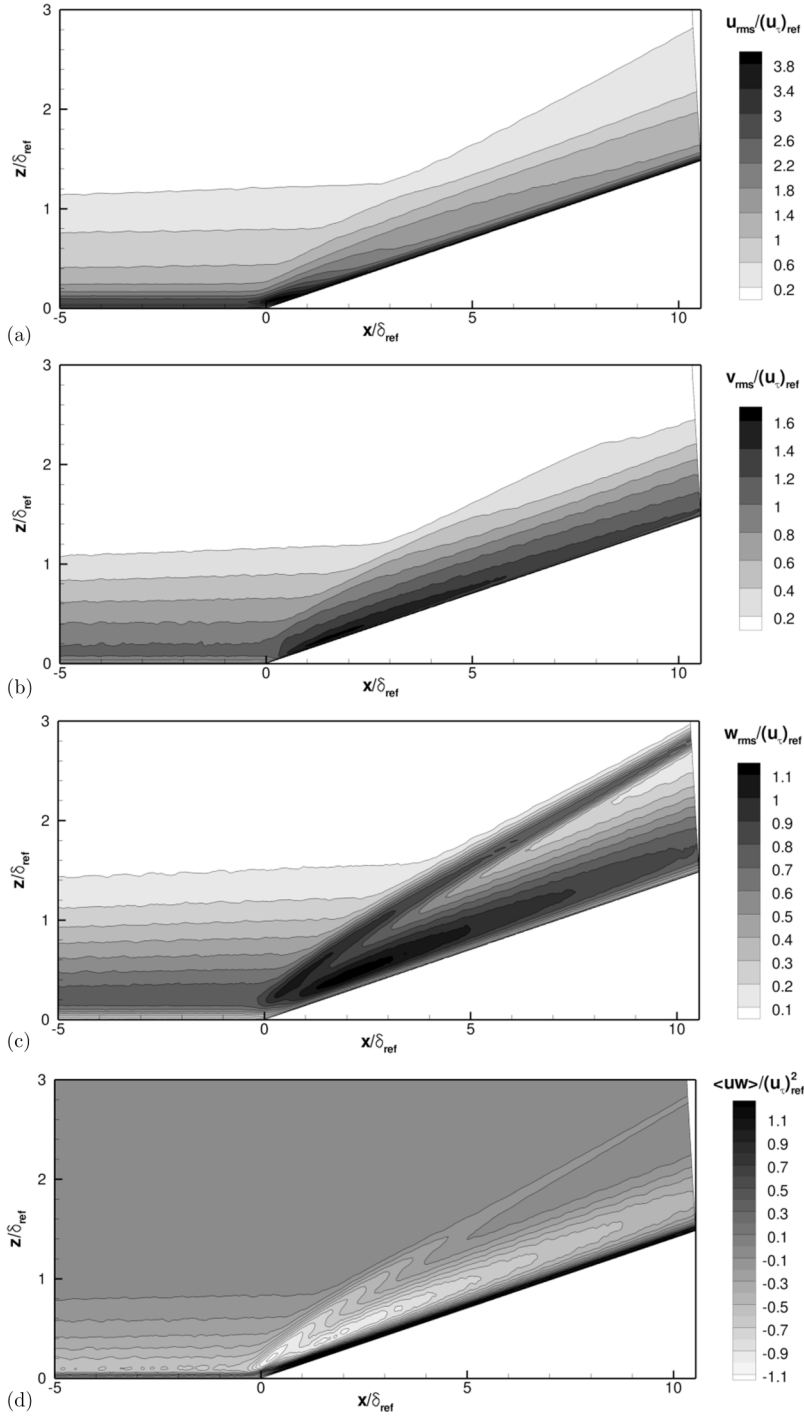
FIG. 18. Time- and spanwise-averaged contours of the (a) streamwise velocity fluctuation intensity $\sqrt{\widetilde{u''u''}}/u_{\tau,\text{ref}}$, (b) spanwise velocity fluctuation intensity $\sqrt{\widetilde{v''v''}}/u_{\tau,\text{ref}}$, (c) wall-normal velocity fluctuation intensity $\sqrt{\widetilde{w''w''}}/u_{\tau,\text{ref}}$, and (d) Reynolds shear stress $\widetilde{u''w''}/u_{\tau,\text{ref}}^2$. The normalization is by the upstream friction velocity obtained at the recycling station of the auxiliary DNS, which is equivalent to the inlet of the principal DNS.
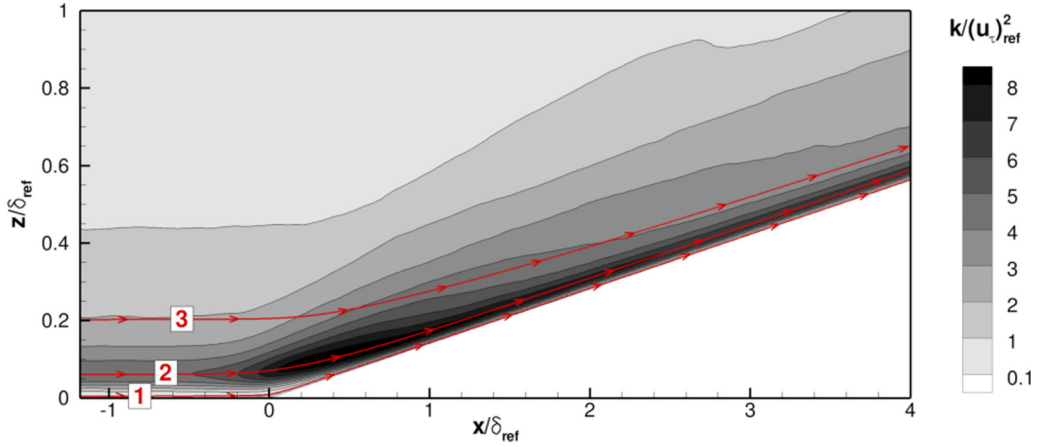
FIG. 19. Time- and spanwise-averaged field of the Favre-averaged turbulent kinetic energy. The three streamlines used in Fig. 23 are also shown.
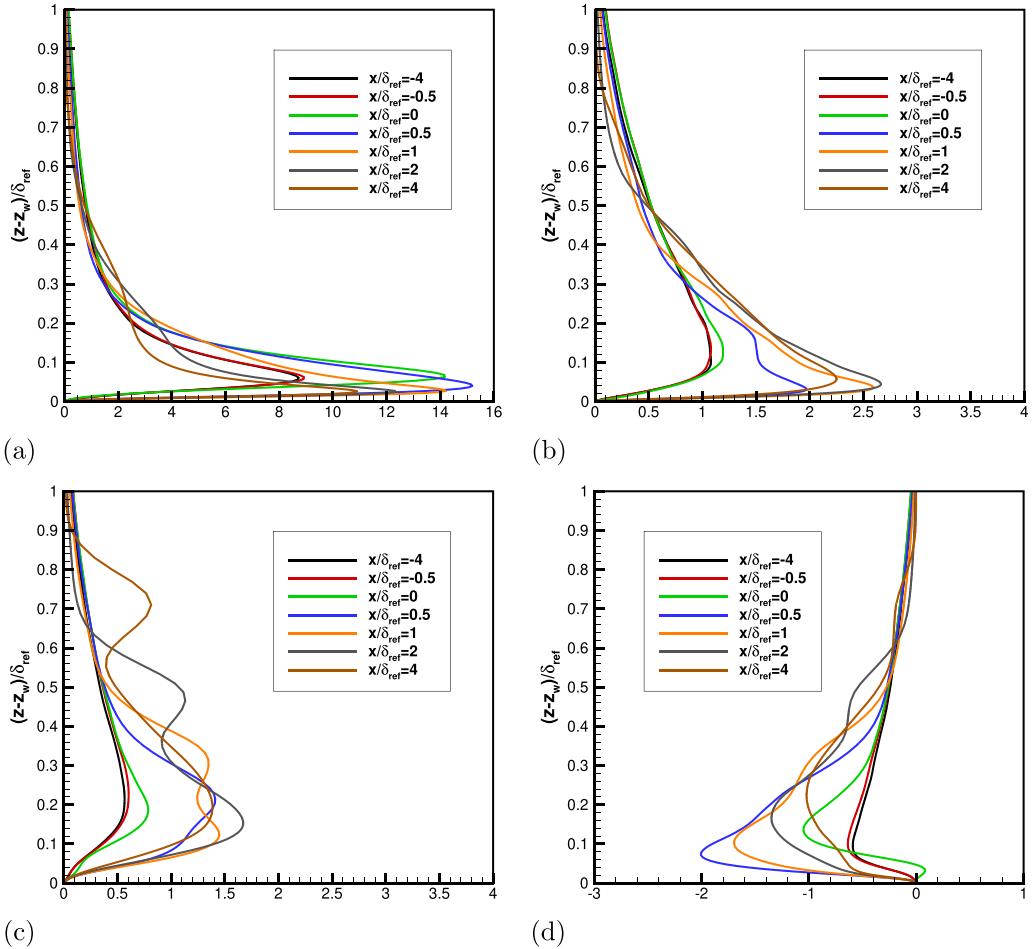

FIG. 20. Reynolds stress profiles at several locations through the interaction (a) $\widetilde{u_r'' u_r''}/u_{\tau,\text{ref}}^2$, (b) $\widetilde{v_r'' v_r''}/u_{\tau,\text{ref}}^2$, (c) $\widetilde{w_r'' w_r''}/u_{\tau,\text{ref}}^2$, and (d) $\widetilde{u_r'' w_r''}/u_{\tau,\text{ref}}^2$.
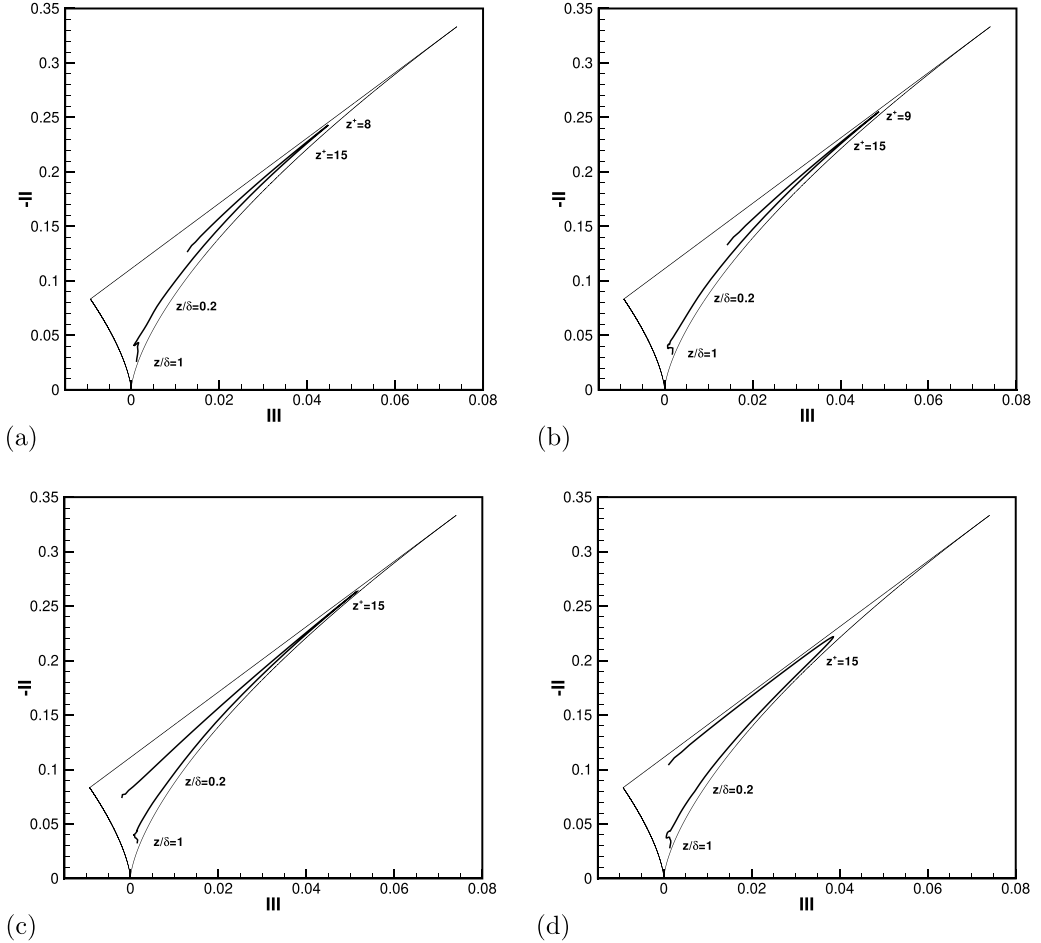
FIG. 21. Lumley triangles. Each subfigure shows the trace of the invariant pair $(-\mathrm{II},\mathrm{III})$ of the Reynolds stress anisotropy tensor as a function of the wall-normal coordinate, z, for a fixed streamwise location, x: (a) $x/\delta = -4.0$, (b) $x/\delta = -0.25$, (c) $x/\delta = 0.0$, and (d) $x/\delta = 0.5$.

of the Reynolds stress in the downstream flow to the maximum value in the upstream flow. The observed values of A are $A_{11} = 1.82$, $A_{22} = 2.53$, $A_{33} = 2.28$, and $A_{13} = 2.12$, i.e., the strongest amplification is in the spanwise component, followed by the wall-normal component, and the weakest amplification is in the streamwise component. The PIV measurements of Schreyer *et al.* [4] also show that the streamwise fluctuations are amplified less than the wall-normal fluctuations.

The shock causes a decrease in u and an increase in w. Consequently, it is associated with a negative shear stress [see Fig. 18(d)]. As typically observed in supersonic STBLIs (see, e.g., [43]), the shock is associated with a strong peak in $\widetilde{w''w''}$. The reason for this is that the average w, which is close to zero in the upstream boundary layer (there is only a small positive component due to the displacement effect of the boundary layer), jumps to a large positive value across the shock due to the deflection of the flow. As a result, any difference between the instantaneous and the average shock position leads to a relatively strong fluctuation w'', which explains the peak in $\widetilde{w''w''}$.

Figure 19 shows contours of the TKE $\frac{\widetilde{u_i''u_i''}}{2}$ through the interaction. It is apparent that the locus of points where the maximum values of TKE occur in the boundary layer coincides with a mean streamline (streamline 2 in Fig. 19, which coincides with the wall-normal location of the inner
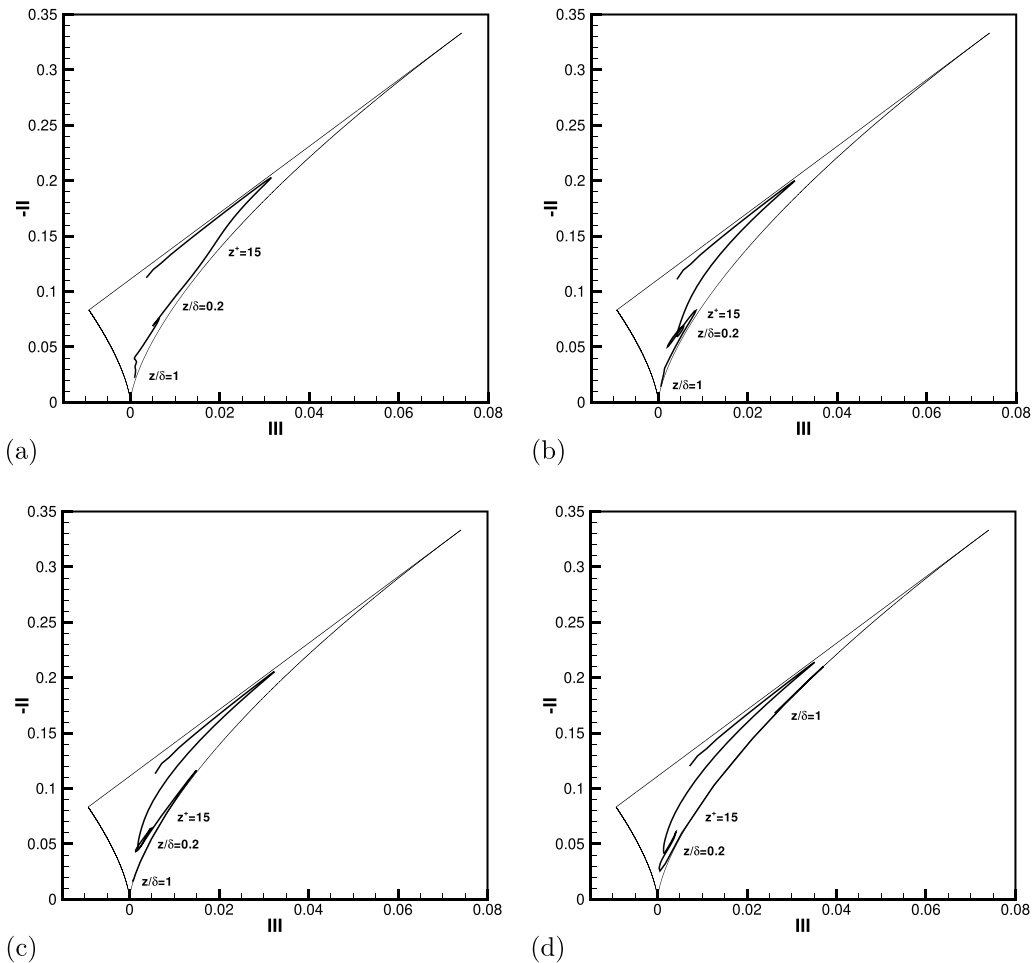
FIG. 22. Lumley triangles as in Fig. 21 but at the streamwise locations: (a) $x/\delta = 1.0$, (b) $x/\delta = 2.0$, (c) $x/\delta = 3.0$, and (d) $x/\delta = 5.0$.

fluctuation peak in the upstream boundary layer). This may be compared with the behavior typically seen in separated supersonic interactions, where a detached shear layer is formed. In the flow downstream of the shock, the peak Reynolds stresses and TKE values are then found farther away from the wall. Note that in the present attached flow, the structure of the Reynolds stresses and TKE does change somewhat as we move downstream. The contour lines of, e.g., $\widetilde{u''u''}$ and TKE bulge toward higher wall-normal locations z between $x/\delta \approx 0$–5, which indicates a broadening of the fluctuation peak and is consistent with increased activity away from the wall as is typically seen in adverse pressure gradient flows. This is also apparent from the Reynolds stress profiles in Fig. 20. The profiles of the streamwise component, for example, show a slight broadening of the fluctuation peak including increased fluctuations away from the wall. However, the wall-normal location of the fluctuation peak remains close to the wall. At the corner, the peak is located only slightly farther away from the wall than in the incoming boundary layer. Note that the fluctuation peak is probably expected to remain close to the wall since the low-speed region at the corner is thin and the inflection point in the velocity profiles is located close to the wall.

The Reynolds stress anisotropy tensor b_{ij} is defined as $b_{ij} = \frac{\widetilde{u_i''u_j''}}{2k} - \frac{\delta_{ij}}{3}$, where $k = \frac{\widetilde{u_i''u_i''}}{2}$ is the turbulent kinetic energy and δ_{ij} is the Kronecker function. The second and third invariants of the
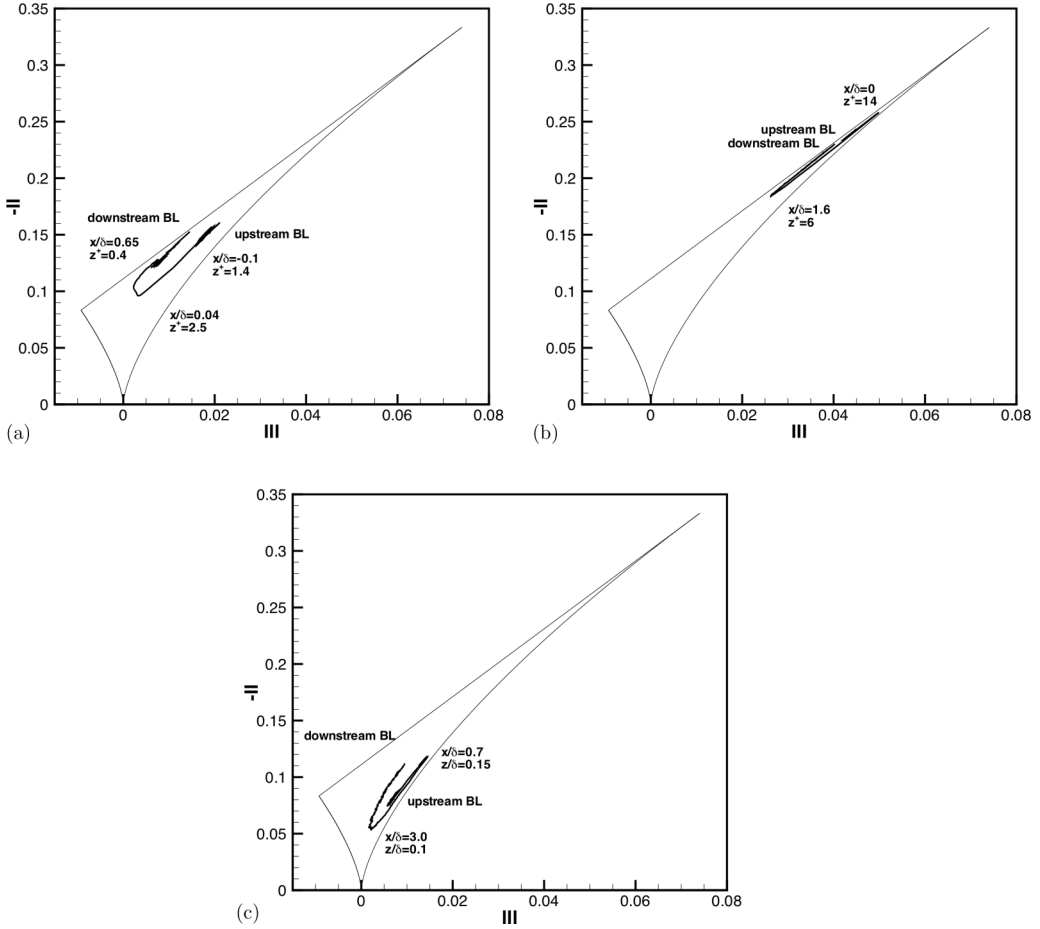
FIG. 23. Traces of the invariant pair $(-\text{II},\text{III})$ of the Reynolds stress anisotropy tensor along three mean-flow streamlines: (a) along the streamline passing through $z^+ = 1$ at $x/\delta = -4$, (b) along the streamline passing through $z^+ = 12$ at $x/\delta = -4$, and (c) along the streamline passing through $z/\delta = 0.2$ at $x/\delta = -4$. See also Fig. 19 for the location of the streamlines.

anisotropy tensor are $\text{II} = -\frac{b_{ij}b_{ji}}{2}$ and $\text{III} = \frac{b_{ij}b_{jk}b_{ki}}{3}$ (the first invariant, which is the trace, is zero). As shown by Lumley and Newman [44] and Choi and Lumley [45], realizability imposes constraints on the possible values of II and III. In the $(-\text{II},\text{III})$-plane, the realizability region is enclosed in a "triangular" boundary, referred to as the Lumley triangle.

Figure 21(a) shows the Lumley triangle and the trace of the invariant pair $(-\text{II},\text{III})$ as a function of the wall-normal coordinate z in the undisturbed boundary layer of the present DNS. Near the wall ($z^+ < 8$), the invariants follow the top boundary of the Lumley triangle, which corresponds to two-component turbulence. In this near-wall region, the normal fluctuations w'' are damped by the presence of the wall. Since the streamwise component becomes more dominant as z is increased, the invariant pair moves toward the top right corner of the Lumley triangle, which corresponds to one-component turbulence. As z is increased further, the invariant pair moves along the bottom right boundary of the Lumley triangle, which corresponds to axisymmetric turbulence with one of the components (in this case, u'') being larger than the other two. At the edge of the boundary layer ($z/\delta = 1$), the invariant pair is close to the bottom corner of the Lumley triangle, which corresponds to an isotropic Reynolds stress tensor. The trace of the invariant pair is typical for attached shear
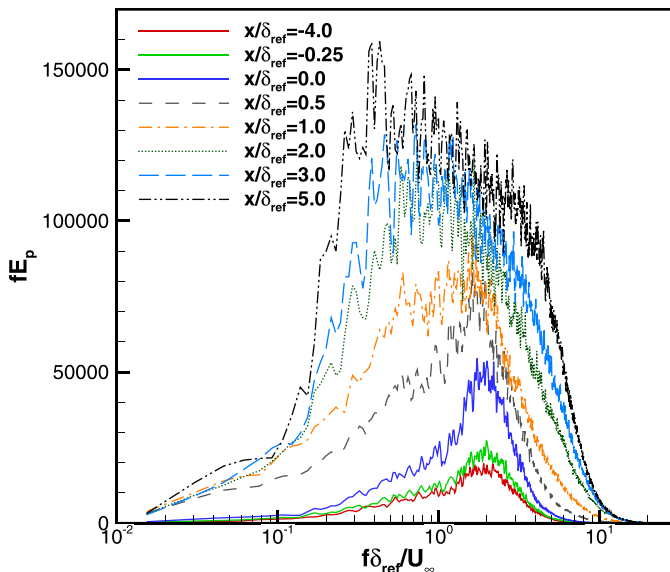
FIG. 24. Premultiplied spectra of wall pressure fluctuations at several streamwise locations.

layers. A qualitatively identical behavior is shown in [46] (Fig. 11.1) for incompressible channel flow, and in [42,47] for supersonic boundary layers.

As is apparent from Figs. 21 and 22, the anisotropy of the Reynolds stress tensor changes through the interaction. The evolution of the invariant pair along three streamlines is shown in Fig. 23: the first streamline is located close to the wall (it passes through $z^+ = 1$ at $x/\delta = -4.0$), the second is located at the inner-peak location in the upstream boundary layer (it passes through $z^+ = 12$ at $x/\delta = -4.0$), and the third is located in the log layer in the upstream boundary layer (it passes through $z/\delta = 0.2$ at $x/\delta = -4.0$). It is apparent from Fig. 23 that the invariant pair $(-\mathrm{II},\mathrm{III})$ traces a "U"-shape as the streamwise coordinate is increased through the interaction. The anisotropy first moves toward the origin of the Lumley triangle before then relaxing away from it again. The movement toward the origin occurs because both $-\mathrm{II}$ and III decrease as the turbulence is subjected to the adverse pressure gradient and becomes more isotropic. This behavior is also visible by looking at the Lumley triangles at several locations through the interaction (Figs. 21 and 22): it is apparent, especially in Figs. 22(b)–22(d), that the invariant trace is pulled toward the origin of the Lumley triangle. The main physics shown in these plots is thus the effect of the shock and adverse pressure gradient on the anisotropy of the velocity fluctuations, which become more isotropic in the interaction. Lumley triangles for an incipiently separated transonic STBLI [42] and a separated supersonic STBLI [47] have also previously shown that the fluctuations become more isotropic in the near-wall region in the interaction.

Figure 24 shows the wall pressure spectra in the upstream boundary layer and at several locations around the corner and on the ramp. The signals were sampled at a frequency of approximately $f_s \delta/U_\infty = 126$. A single broadband peak is maintained at all locations, but with the following changes: (i) The rms of the wall pressure fluctuations increases, which is shown by the increase in the area under the (premultiplied and non-normalized) spectra. At $x/\delta = 5.0$, for example, $p_{w,\mathrm{rms}}/p_\infty = 0.51$ compared to 0.13 in the upstream boundary layer. (ii) The central frequency of the broadband peak shifts to lower values downstream of the shock compared to the upstream boundary layer. At $x/\delta = 5.0$, it is $f\delta/U_\infty \approx 0.9$ compared to $f\delta/U_\infty \approx 2.0$ in the upstream boundary layer. The spectra are resolved down to a low frequency of $f\delta_{\mathrm{ref}}/U_\infty \approx 0.02$, and while they show an increase in low-frequency energy (at, say, $f\delta_{\mathrm{ref}}/U_\infty < 0.1$) downstream of the shock compared to the upstream boundary layer, there is no distinct spectral peak at low frequencies in
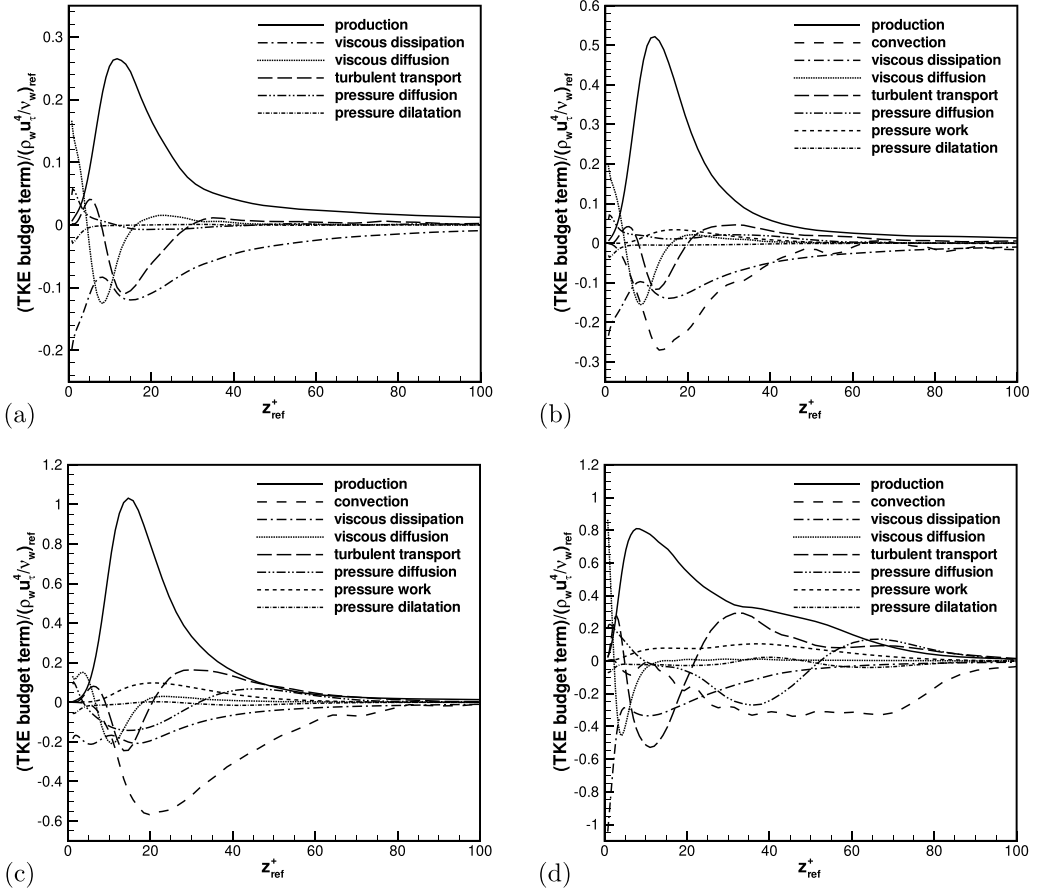
FIG. 25. TKE budget at various streamwise locations: (a) $x/\delta = -4.0$, (b) $x/\delta = -0.25$, (c) $x/\delta = 0.0$, and (d) $x/\delta = 0.5$.

this attached interaction. The absence of significant low-frequency unsteadiness is consistent with observations in supersonic STBLIs. Strong supersonic interactions with mean-flow separation show an energetic, broadband, low-frequency unsteadiness with a central frequency typically in the range $\text{St}_L = fL_{\text{sep}}/U_\infty = 0.02$–$0.05$, where L_{sep} is the separation length (see, e.g., [48,49]). However, weaker cases, including incipiently separated ones, do not show such a distinct and energetic low-frequency spectral peak [43].

The TKE budget in the undisturbed upstream boundary layer ($x/\delta = -4$) is given in Fig. 25(a). Note that the TKE budget terms are defined here as in Ref. [50], p. 247. As typically seen in attached boundary layers (see, e.g., [36,37]), viscous diffusion and dissipation are the dominant terms in the viscous sublayer, where they balance (with smaller contributions coming from pressure diffusion and dilatation). The production peak is at $z^+ \approx 15$ and is balanced by viscous dissipation, turbulent transport, and viscous diffusion. In the log layer and the outer part of the boundary layer, production and dissipation balance. As the corner is approached, the magnitude of the peak production increases significantly [see Figs. 25(b) and 25(c) at $x/\delta = -0.25, 0$]. The additional production is balanced primarily by an additional convection term contribution that is present near the corner. Further downstream at $x/\delta = 0.5$ and 1 [Figs. 25(d) and 26(a)], significant contributions of the pressure diffusion term, the convection term, and the turbulent transport are seen in the region $z^+ = 20$–100. At the farthest locations downstream [$x/\delta = 3$ and 5; see Figs. 26(c) and 26(d)], the inner part of
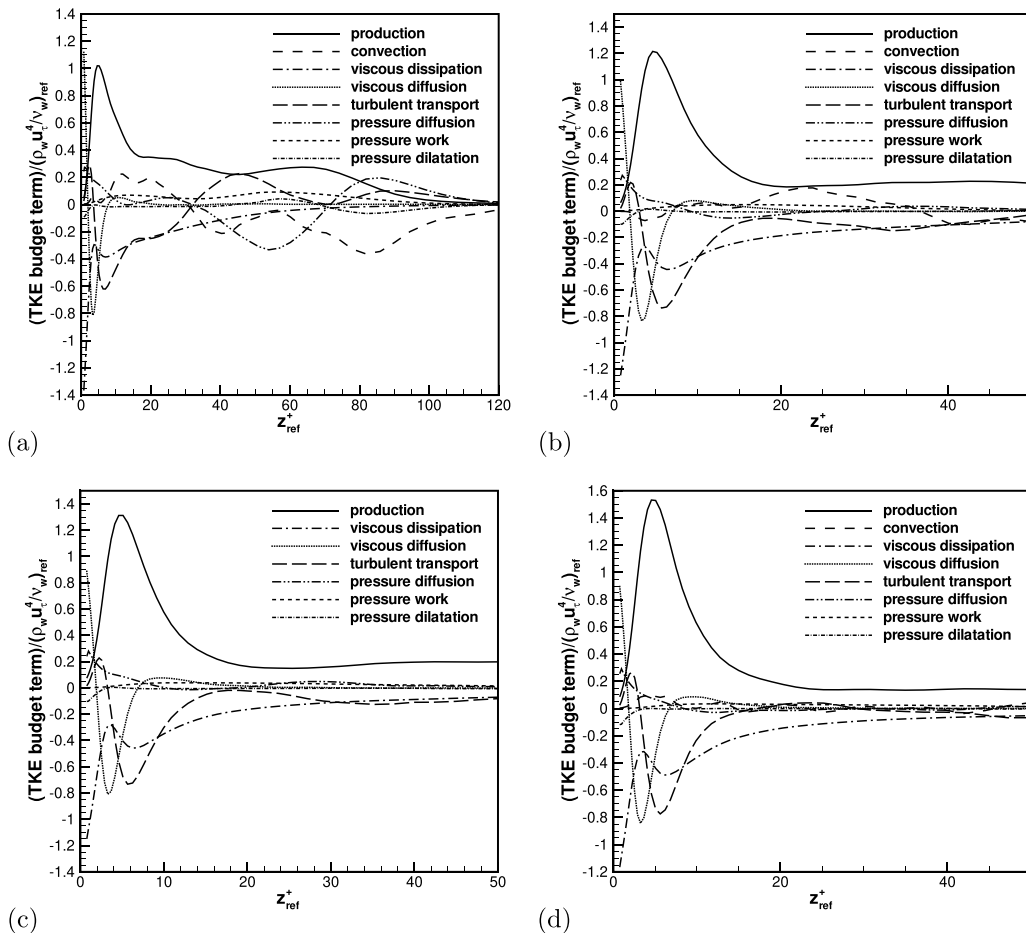
FIG. 26. TKE budget at various streamwise locations: (a) $x/\delta = 1.0$, (b) $x/\delta = 2.0$, (c) $x/\delta = 3.0$, and (d) $x/\delta = 5.0$.

the boundary layer recovers to an equilibrium state with the balances mentioned in the description of Fig. 25(a) at work.

While Figs. 26(b)–26(d) focus on the near-wall region, Fig. 27 shows one of the profiles, at $x/\delta = 5.0$, on a larger wall-normal scale. The region between $z^+ = 130$ and 220, where significant variations in the TKE budget terms occur, is associated with the shock. The behavior in this region is due to the unsteadiness of the shock, which smoothes the shock jump in the mean, generates a local fluctuation peak (e.g., Fig. 18), and leads to the budget terms shown in Fig. 27.

6. Surface heat flux and the turbulent temperature field

Standard RANS models typically do not predict hypersonic STBLIs accurately. The prediction of the surface heat flux is particularly difficult, as discussed in the Introduction. For example, Roy and Blottner [20] conclude that "while some of the turbulence models do provide reasonable predictions for the surface pressure, the predictions for surface heat flux are generally poor, and often in error by a factor of four or more."

We have verified several scalings linking the velocity field to the temperature field. The simplest is probably the Reynolds analogy (RA), which links the mean skin friction coefficient, C_f, to
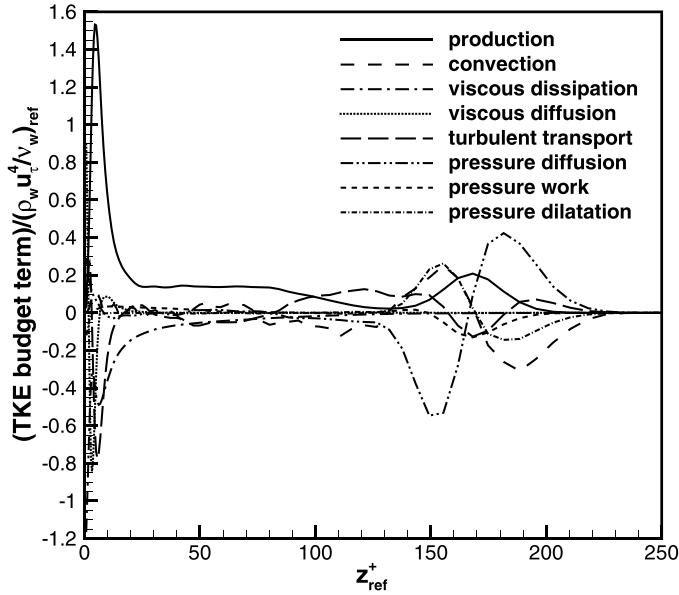
FIG. 27. TKE budget at $x/\delta = 5.0$ and on a larger wall-normal scale than in Fig. 26(d) to show the shock region.

the mean Stanton number, C_h: RAF $= \frac{2C_h}{C_f} = $ const ≈ 1. Figure 28(a) shows the Reynolds analogy factor (RAF) as a function of the streamwise coordinate, x, through the interaction. The Reynolds analogy is satisfied in the undisturbed upstream boundary layer, where RAF ≈ 1.2, which is within the range $0.9 < $ RAF < 1.3 typically observed in hypersonic zero-pressure-gradient boundary layers [20]. The most significant departures from this range occur around the corner, between $x/\delta = -0.5$ and $x/\delta = 2$, where RAF $\gg 1$. The Reynolds analogy factor peaks at the corner, where RAF $= 5.2$. As is apparent from Fig. 11, this is due to the fact that the skin friction coefficient approaches zero at the corner since the flow is close to separation, whereas the heat transfer coefficient does not. The value of RAF remains above the typical range for zero-pressure-gradient
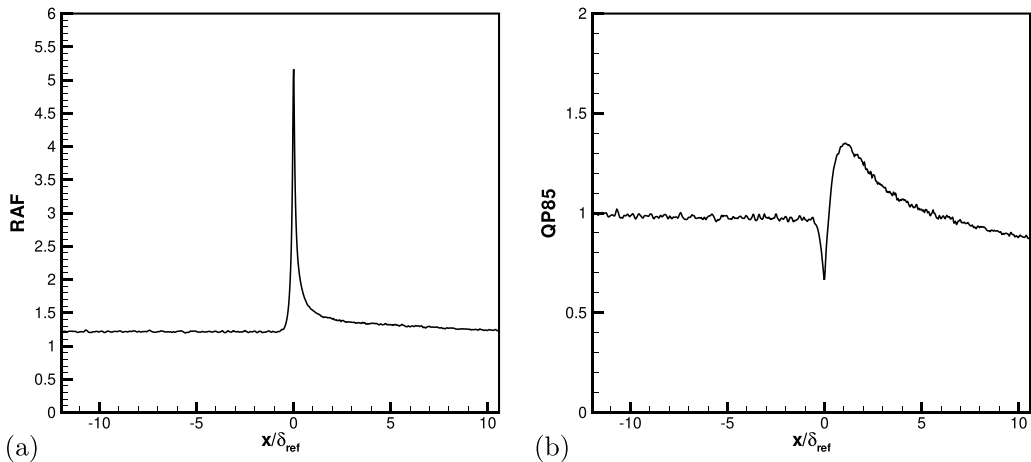

FIG. 28. Surface heat-transfer scalings through the interaction: (a) Reynolds analogy and (b) QP85 scaling.
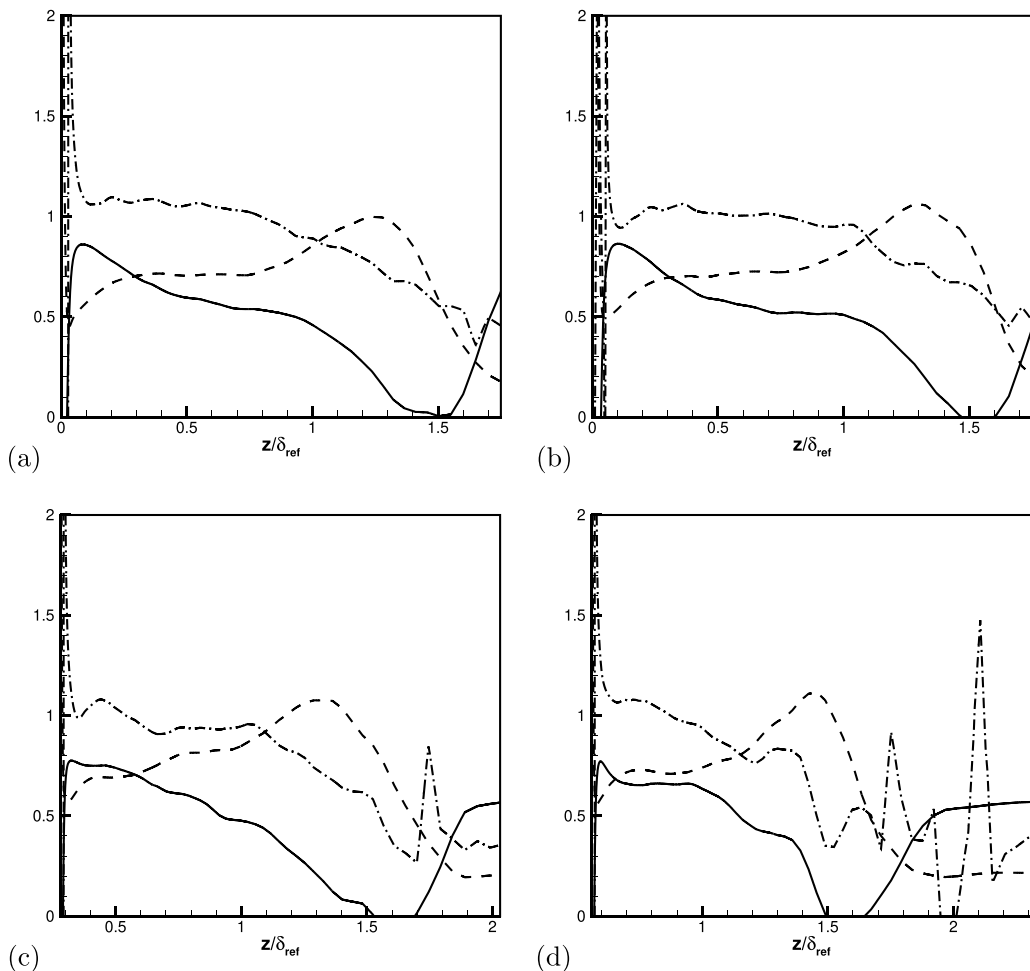
FIG. 29. Profiles of the SRA relations at various streamwise locations. SRA phase $R_{uT} = -\frac{\widetilde{u''T''}}{u''_{\mathrm{rms}}T''_{\mathrm{rms}}}$ (solid), SRA magnitude $\frac{1}{(\gamma-1)M^2}\frac{\tilde{u}}{u''_{\mathrm{rms}}}\frac{T''_{\mathrm{rms}}}{\tilde{T}}$ (dashed), and modified SRA magnitude $\frac{1}{(\gamma-1)M^2}\frac{\tilde{u}}{u''_{\mathrm{rms}}}\frac{T''_{\mathrm{rms}}}{\tilde{T}}\mathrm{Pr}_t(1-\frac{\partial\tilde{T}_t}{\partial\tilde{T}})$ (dash-dot). (a) $x/\delta = -4.0$, (b) $x/\delta = 0.0$, (c) $x/\delta = 2.0$, and (d) $x/\delta = 4.0$.

boundary layers for a significant distance downstream of the corner—it is RAF = 1.53 at $x/\delta = 1.0$, 1.41 at $x/\delta = 2.0$, 1.34 at $x/\delta = 4.0$—before dropping to RAF < 1.3 downstream of $x/\delta = 5.75$.

Disagreement with the Reynolds analogy in hypersonic STBLI has previously been observed in the literature, especially for separated cases. The heat transfer tends to scale better with the wall pressure, rather than the skin friction, in these cases [8,12,16–18]. As shown in Fig. 28(b), the present DNS results show reasonable agreement with the QP85 scaling [18]: QP85 = $\frac{q(x)}{q_u}(\frac{p_u}{p(x)})^{0.85} \approx$ const ≈ 1, where the subscript "u" denotes upstream values. This scaling has previously been shown to match experiments of hypersonic STBLI (see, e.g., [12,17]). As is apparent from Fig. 28(b), there are some departures from the scaling in the regions of strongest adverse pressure gradient in the vicinity of the corner, where the minimum value of QP85 is 0.65 and the maximum value is 1.35, but the general agreement is good and the singularity at the corner is reduced compared to the Reynolds analogy.

The strong Reynolds analogy (SRA) links the temperature fluctuations T'' to the velocity fluctuations u'' [51]. According to the SRA, $R_{uT} = -\frac{\widetilde{u''T''}}{u''_{\mathrm{rms}}T''_{\mathrm{rms}}} \approx 1$ (phase relationship) and
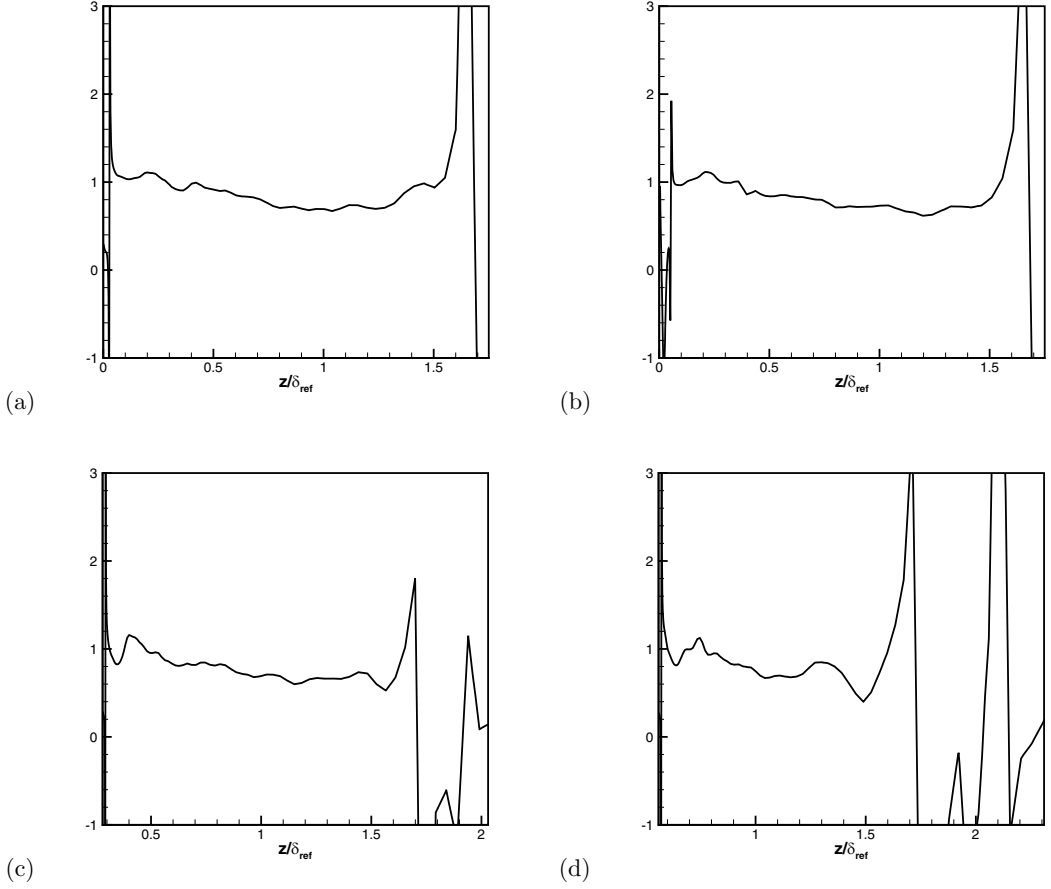
FIG. 30. Profiles of the turbulent Prandtl number $\mathrm{Pr}_t = \frac{\overline{\rho u'' w''}}{\overline{\rho T'' w''}} \frac{\partial \tilde{T}/\partial z}{\partial \tilde{u}/\partial z}$ at various streamwise locations: (a) $x/\delta = -4.0$, (b) $x/\delta = 0.0$, (c) $x/\delta = 2.0$, and (d) $x/\delta = 4.0$.

$\frac{1}{(\gamma-1)M^2} \frac{\tilde{u}}{u''_{\mathrm{rms}}} \frac{T''_{\mathrm{rms}}}{\tilde{T}} \approx 1$ (magnitude relationship). It is apparent from Fig. 29(a) that in the upstream boundary layer, $R_{uT} \approx 0.6$ across most of the boundary layer, as is typically seen in attached zero-pressure-gradient compressible boundary layers. The magnitude relation, however, is low at 0.5–0.8 across the boundary layer. This is consistent with the observations of Duan *et al.* [36] and may be attributed to the cold wall temperature in the DNS. The modified SRA magnitude relation of Huang *et al.* [52], $\frac{1}{(\gamma-1)M^2} \frac{\tilde{u}}{u''_{\mathrm{rms}}} \frac{T''_{\mathrm{rms}}}{\tilde{T}} \mathrm{Pr}_t (1 - \frac{\partial \tilde{T}_t}{\partial \tilde{T}})$, accounts for the temperature effect and is close to unity across most of the upstream boundary layer [Fig. 29(a)]. The most significant departures from the SRA occur in the near-wall region, between the wall and the location where the mean temperature $\tilde{T}$ has a maximum (which is at $z/\delta \approx 0.02$ in the upstream boundary layer; see Fig. 15). The phase R_{uT}, for example, is negative near the wall, since $\frac{\partial \tilde{u}}{\partial z} > 0$ and $\frac{\partial \tilde{T}}{\partial z} > 0$ and hence u'' and T'' tend to be correlated rather than anticorrelated. The sign of $\frac{\partial \tilde{T}}{\partial z}$ changes at the wall-normal location where $\tilde{T}$ has a maximum, so that above this location $\frac{\partial \tilde{T}}{\partial z} < 0$ and hence u'' and T'' are anticorrelated and R_{uT} is positive, as typically observed. In the present attached STBLI, the departures from the SRA that are already present in the upstream boundary layer do not become significantly worse as the boundary layer interacts with the shock. As is apparent from Figs. 29(b)–29(d), over most of the boundary layer the phase relation remains around 0.6 through the interaction and the modified
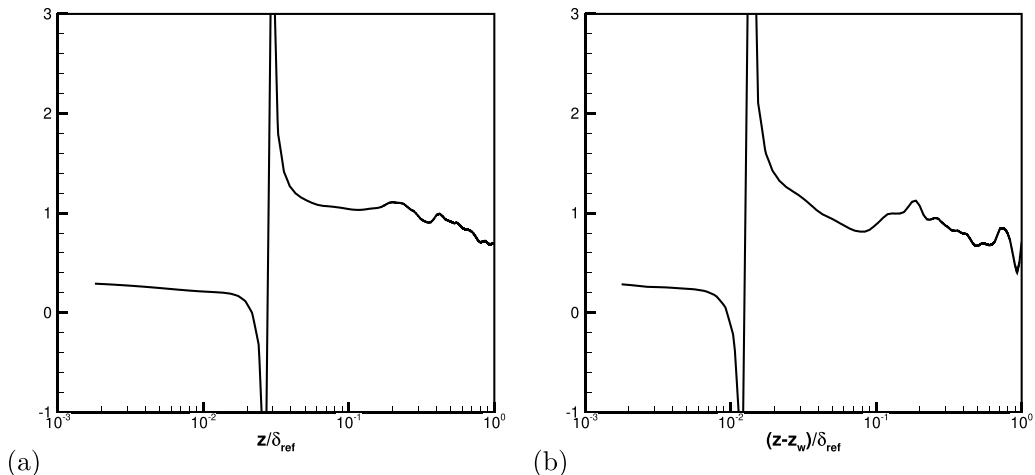
FIG. 31. Pr_t profiles on a semilog scale to highlight the near-wall behavior: (a) $x/\delta = -4.0$ and (b) $x/\delta = 4.0$.

magnitude relation around unity. The profile shapes also remain generally similar downstream of the corner compared to the upstream boundary layer.

In turbulence models, the closure of the momentum equation is usually extended to the energy equation by assuming a constant turbulent Prandtl number: $\mathrm{Pr}_t = \frac{\mu_t C_p}{\kappa_t} = \mathrm{const}$. In other words, the turbulent heat diffusivity κ_t is calculated from the eddy viscosity μ_t as $\kappa_t = (\mu_t C_p)/\mathrm{Pr}_t$, where the turbulence model gives μ_t, and Pr_t is usually taken to be close to 1. Figure 30 shows profiles of $\mathrm{Pr}_t = \frac{\overline{\rho u'' w''}}{\overline{\rho T'' w''}} \frac{\partial \tilde{T}/\partial z}{\partial \tilde{u}/\partial z}$ at several streamwise locations through the interaction. Note that both in the calculation of the SRA relations shown in Fig. 29 and the turbulent Prandtl number shown in Fig. 30, for locations downstream of the corner, all velocity components and gradients have been taken in a ramp-aligned coordinate system (rotated by $8°$). It is apparent that the assumption of a constant Pr_t close to 1 is satisfied reasonably well in most of the outer part of the boundary layer downstream of the corner. At $x/\delta = 4$, for example, Pr_t lies in the range 0.65–1.2 over most of the boundary layer.

However, as shown in Fig. 31, there are more significant differences near the wall. There is a "singularity" with large departures from $\mathrm{Pr}_t \approx 1$ at $z/\delta_{\mathrm{ref}} = 0.025$ in the upstream boundary layer and at $(z - z_w)/\delta_{\mathrm{ref}} = 0.013$ in the downstream boundary layer at $x/\delta_{\mathrm{ref}} = 4.0$. This is due to the fact that $\tilde{T}$ has a maximum, and as a result two of the terms that appear in the Pr_t definition, $\frac{\partial \tilde{T}}{\partial z}$ and $\overline{\rho T'' w''}$, are zero. The maximum of $\tilde{T}$ is the result of two competing effects: the wall heat flux (cold wall) on the one hand, and the viscous heating in the flow on the other. Above the wall-normal location of maximum $\tilde{T}$, Pr_t is approximately 1, whereas below that location, Pr_t is less than 1.

IV. CONCLUSIONS

The hypersonic shock wave/turbulent boundary layer interaction generated by an $8°$ compression ramp in Mach 7.2 flow is investigated using DNS. The observed flow structure is different from that typically seen in supersonic interactions: at the present conditions, the shock angle is shallow (inviscid value $14.3°$). This is typical for hypersonic flows, where the shock angle can be shallow and the layer extending from the wall to the shock can be thin, which is known as a thin shock layer (Ref. [53], pp. 13 and 14). As a result, the DNS shows that the shock foot is immersed in the boundary layer downstream of the corner for a streamwise distance equal to several incoming boundary layer thicknesses before it emerges from the boundary layer, distorted by the passage of the boundary layer structures.

While the flow is found to be attached in the mean, patches of separated flow are observed on an instantaneous basis surrounding the corner. Between $0.15\delta_{ref}$ upstream of the corner and $0.1\delta_{ref}$ downstream, the probability of reversed flow is greater than 20%, which means that the flow is in the ITD (intermittent transitory detachment) state. The maximum probability is 31% at the corner.

The behavior of the turbulence through the interaction is described. The Reynolds stresses are amplified with the streamwise component being less amplified than the other two: R_{uu} is amplified by a factor of 1.82, R_{vv} by a factor of 2.53, R_{ww} by a factor of 2.28, and the shear stress R_{uw} by a factor of 2.12. The fluctuation peak remains close to the wall in the interaction, rather than moving away from the wall. This behavior is consistent with the fact that the low-speed region in the present flow is thin in the wall-normal direction: the region of significant reversed flow probability does not extend above $z/\delta_{ref} \approx 0.05$, and the inflection point in the mean velocity profiles is found at similar wall-normal locations. The anisotropy of the Reynolds stresses changes through the interaction. In the upstream boundary layer, the Lumley triangles show the behavior typically seen in attached zero-pressure-gradient boundary layers. In the interaction region, however, a different structure is seen: both the second and third invariant of the Reynolds stress anisotropy tensor decrease (in other words, the invariant pair is pulled toward the origin), which is consistent with the turbulence becoming more isotropic.

Regarding the heat transfer, it is found that the Reynolds analogy, which relates the skin friction coefficient C_f to the heat transfer coefficient C_h, is not satisfied in the interaction. Large values of the RA factor are observed at the corner, since the flow is close to separation and C_f approaches zero whereas C_h does not. The RA factor then remains above the range of values typically observed in zero-pressure-gradient hypersonic boundary layers for a significant distance downstream of the corner (up to $x/\delta_{ref} = 5.75$). As has previously been reported in the literature in the context of separated hypersonic STBLIs (see, e.g., [12,16,17]), the heat transfer scales better with pressure, rather than skin friction, and the QP85 scaling of Back and Cuffel [18] describes the behavior in the DNS reasonably accurately, although there are departures from it near the corner. In the present attached interaction, the departures from the SRA are relatively weak through the interaction, at least when compared to the behavior of the SRA terms in the upstream boundary layer and provided that the wall heat flux is taken into account by using a modified form of the SRA [52]. The assumption of a constant turbulent Prandtl number around unity is also satisfied reasonably well, although significant departures from it are observed in the near-wall region.

The present DNS data are compared to available experiments, and a good qualitative match is found in terms of the instantaneous and mean-flow structure, as well as for the state of separation.

We expect the DNS to be useful for turbulence modeling, given the known deficiencies of turbulence models in hypersonic STBLIs even for attached cases (see [20–22]). In the present work, we provide quantities relevant for turbulence modeling, such as mean and fluctuating fields, Reynolds stresses, the anisotropy tensor, TKE budgets, and the turbulent Prandtl number.

[1] V. Mikulla and C. C. Horstman, Turbulence measurements in hypersonic shock-wave boundary-layer interaction flows, AIAA J. **14**, 568 (1976).

[2] P. B. Bookey, C. Wyckham, A. J. Smits, and M. P. Martin, New experimental data of STBLI at DNS/LES accessible Reynolds numbers, AIAA paper 2005-309, 2005.

[3] A.-M. Schreyer, D. Sahoo, and A. J. Smits, Experimental investigations of a hypersonic shock turbulent boundary layer interaction, AIAA paper 2011-481, 2011.

[4] A.-M. Schreyer, D. Sahoo, O. J. H. Williams, and A. J. Smits, Experimental investigation of two hypersonic shock/turbulent boundary-layer interactions, AIAA J. **56**, 4830 (2018).

[5] F. F. J. Schrijer, F. Scarano, and B. W. van Oudheusden, Application of PIV in a Mach 7 double-ramp flow, Exp. Fluids **41**, 353 (2006).

[6] J. Brooks, A. K. Gupta, C. Helm, M. P. Martín, M. Smith, and E. Marineau, Mach 10 PIV flow field measurements of a turbulent boundary layer and shock turbulent boundary layer interaction, AIAA paper 2017-3325, 2017.

[7] G. M. Elfstrom, Turbulent hypersonic flow at a wedge-compression corner, J. Fluid Mech. **53**, 113 (1972).

[8] G. T. Coleman and J. L. Stollery, Heat transfer from hypersonic turbulent flow at a wedge compression corner, J. Fluid Mech. **56**, 741 (1972).

[9] M. I. Kussoy and C. C. Horstman, An experimental documentation of a hypersonic shock-wave turbulent boundary layer interaction flow – with and without separation, Tech. Rep. TM X-62412 (NASA, 1975).

[10] M. I. Kussoy and C. C. Horstman, Documentation of two- and three-dimensional hypersonic shock wave/turbulent boundary layer interaction flows, Tech. Rep. TM 101075 (NASA, 1989).

[11] M. I. Kussoy and C. C. Horstman, Documentation of two- and three-dimensional shock-wave/turbulent-boundary-layer interaction flows at Mach 8.2, Tech. Rep. TM 103838 (NASA, 1991).

[12] M. S. Holden, Shock wave turbulent boundary layer interaction in hypersonic flow, Tech. Rep. ARL TR 75-0204 (Aerospace Research Laboratories, 1975).

[13] M. S. Holden, Studies of the mean and unsteady structure of turbulent boundary layer separation in hypersonic flow, AIAA paper 91-1778, 1991.

[14] M. S. Holden, J. R. Moselle, S. J. Sweet, and S. C. Martin, A database of aerothermal measurements in hypersonic flow for CFD validation, AIAA paper 96-4597, 1996.

[15] M. Holden, M. MacLean, T. Wadhams, and E. Mundy, Experimental studies of shock wave/turbulent boundary layer interaction in high Reynolds number supersonic and hypersonic flows to evaluate the performance of CFD codes, AIAA paper 2010-4468, 2010.

[16] E. Schülein, Skin-friction and heat flux measurements in shock/boundary-layer interaction flows, AIAA J. **44**, 1732 (2006).

[17] N. Murray, R. Hillier, and S. Williams, Experimental investigation of axisymmetric hypersonic shock-wave/turbulent-boundary-layer interactions, J. Fluid Mech. **714**, 152 (2013).

[18] L. H. Back and R. F. Cuffel, Changes in heat transfer from turbulent boundary layers interacting with shock waves and expansion waves, AIAA J. **8**, 1871 (1970).

[19] D. V. Gaitonde, Progress in shock wave/boundary layer interactions, Prog. Aerosp. Sci. **72**, 80 (2015).

[20] C. J. Roy and F. G. Blottner, Review and assessment of turbulence models for hypersonic flows, Prog. Aerosp. Sci. **42**, 469 (2006).

[21] P. A. Gnoffo, S. A. Berry, and J. W. Van Norman, Uncertainty assessments of 2D and axisymmetric hypersonic shock wave - turbulent boundary layer interaction simulations at compression corners, 42nd AIAA Thermophysics Conference paper 2011-3142, 2011.

[22] J. L. Brown, Shock wave impingement on boundary layers at hypersonic speeds: Computational analysis and uncertainty, 42nd AIAA Thermophysics Conference paper 2011-3143, 2011.

[23] D. Knight and M. Mortazavi, Simulation of non-equilibrium hypersonic shock wave boundary layer interactions using the Navier-Stokes equations, Tech. Rep. CCD Report 2018-1 (Rutgers University, 2018).

[24] G. S. Settles and L. J. Dodson, Hypersonic shock/boundary-layer interaction database, Tech. Rep. CR-177577 (NASA, 1991).

[25] G. S. Settles and L. J. Dodson, Hypersonic shock/boundary-layer interaction database: New and corrected data, Tech. Rep. CR-177638 (NASA, 1994).

[26] G. S. Settles and L. J. Dodson, Supersonic and hypersonic shock/boundary-layer interaction database, AIAA J. **32**, 1377 (1994).

[27] M. P. Martín, E. M. Taylor, M. Wu, and V. G. Weirs, A bandwidth-optimized WENO scheme for the effective direct numerical simulation of compressible turbulence, J. Comput. Phys. **220**, 270 (2006).

[28] E. M. Taylor, M. Wu, and M. P. Martín, Optimization of nonlinear error for weighted essentially non-oscillatory methods in direct numerical simulations of compressible turbulence, J. Comput. Phys. **223**, 384 (2007).

[29] J. H. Williamson, Low-storage Runge-Kutta schemes, J. Comput. Phys. **35**, 48 (1980).

[30] F. G. Keyes, A summary of viscosity and heat-conduction data for He, A, H_2, O_2, N_2, CO, CO_2, H_2O, and air, Trans. ASME **73**, 589 (1951).

[31] S. Xu and M. P. Martín, Assessment of inflow boundary conditions for compressible turbulent boundary layers, Phys. Fluids **16**, 2623 (2004).

[32] M. Wu and M. P. Martín, Direct numerical simulation of supersonic turbulent boundary layer over a compression ramp, AIAA J. **45**, 879 (2007).

[33] M. Ringuette, M. Wu, and M. P. Martín, Low Reynolds number effects in a Mach 3 shock/turbulent-boundary-layer interaction, AIAA J. **46**, 1884 (2008).

[34] S. Priebe, M. Wu, and M. P. Martín, Direct numerical simulation of a reflected-shock-wave/turbulent-boundary-layer interaction, AIAA J. **47**, 1173 (2009).

[35] M. P. Martín, Direct numerical simulation of hypersonic turbulent boundary layers. Part 1. Initialization and comparison with experiments, J. Fluid Mech. **570**, 347 (2007).

[36] L. Duan, I. Beekman, and M. P. Martín, Direct numerical simulation of hypersonic turbulent boundary layers. Part 2. Effect of wall temperature, J. Fluid Mech. **655**, 419 (2010).

[37] L. Duan, I. Beekman, and M. P. Martín, Direct numerical simulation of hypersonic turbulent boundary layers. Part III: Effect of Mach number, J. Fluid Mech. **672**, 245 (2011).

[38] S. Priebe, Direct numerical simulation of two shock wave/turbulent boundary layer interactions, Ph.D. thesis, Princeton University, 2012.

[39] S. Priebe and M. P. Martín, Direct numerical simulation of a hypersonic turbulent boundary layer on a large domain, AIAA paper 2011-3432, 2011.

[40] R. L. Simpson, Turbulent boundary-layer separation, Annu. Rev. Fluid Mech. **21**, 205 (1989).

[41] Y. Na and P. Moin, Direct numerical simulation of a separated turbulent boundary layer, J. Fluid Mech. **374**, 379 (1998).

[42] S. Pirozzoli, M. Bernardini, and F. Grasso, Direct numerical simulation of transonic shock/boundary layer interaction under conditions of incipient separation, J. Fluid Mech. **657**, 361 (2010).

[43] S. Piponniau, J. P. Dussauge, J. F. Debiève, and P. Dupont, A simple model for low-frequency unsteadiness in shock-induced separation, J. Fluid Mech. **629**, 87 (2009).

[44] J. L. Lumley and G. R. Newman, The return to isotropy of homogeneous turbulence, J. Fluid Mech. **82**, 161 (1977).

[45] K.-S. Choi and J. L. Lumley, The return to isotropy of homogeneous turbulence, J. Fluid Mech. **436**, 59 (2001).

[46] S. B. Pope, *Turbulent Flows* (Cambridge University Press, Cambridge, 2000).

[47] M. Grilli, S. Hickel, and N. A. Adams, Large-eddy simulation of a supersonic turbulent boundary layer over a compression-expansion ramp, Int. J. Heat Fluid Flow **42**, 79 (2013).

[48] J.-P. Dussauge, P. Dupont, and J.-F. Debiève, Unsteadiness in shock wave boundary layer interactions with separation, Aerosp. Sci. Technol. **10**, 85 (2006).

[49] N. T. Clemens and V. Narayanaswamy, Low-frequency unsteadiness of shock wave/turbulent boundary layer interactions, Annu. Rev. Fluid Mech. **46**, 469 (2014).

[50] D. C. Wilcox, *Turbulence Modeling for CFD*, 3rd ed. (DCW Industries, 2006).

[51] M. V. Morkovin, Effects of compressibility on turbulent flows, in *Mécanique de la Turbulence* (1962), pp. 367–380.

[52] P. G. Huang, G. N. Coleman, and P. Bradshaw, Compressible turbulent channel flows: DNS results and modelling, J. Fluid Mech. **305**, 185 (1995).

[53] J. D. Anderson, *Hypersonic and High-temperature Gas Dynamics*, 2nd ed. (AIAA Education Series, Reston, Virginia, 2006).